The extension of Rietveld refinement for benchtop powder XRD analysis of ultra-small supported nanoparticles

Jeremiah Lipp[1*], Ritubarna Banerjee[1], M.D. Fakhruddin Patwary[1], Nirmalendu Patra[2], Anhua Dong[1], Frank Girgsdies[3], Simon R. Bare[2], J.R. Regalbuto[1]

[1]*University of South Carolina, Columbia, SC, 29201, United States*

[2]*SLAC National Accelerator Laboratory, Menlo Park, CA, 94025, United States*

[3]*Fritz Haber Institute of the Max Planck Society, Department of Inorganic Chemistry, 14195 Berlin, Germany*

Email: jlipp@email.sc.edu

Abstract

We present a method for characterizing ultra-small (< 2nm) supported crystallites with benchtop XRD. Central to the method is an understanding of the intensity effects at play; these intensity effects and their corrections are discussed in depth. Background subtraction – long considered one of the main barriers to ultra-small crystal characterization – is solved by correcting the diffractogram of a separately measured support for the relevant intensity effects. Rietveld refinement is demonstrated to be an adequate analysis method for the general characterization of simple nano-systems. A 4.8% Pt / SiO_2 sample (1.3 nm, volume-weighted average) is used as a case study; it is found that the Pt spontaneously oxidizes under ambient conditions and consists of a metallic core surrounded by a PtO_2 shell. Both phases have average dimensions smaller than 1 nm. The XRD results also suggest lattice expansion of the Pt core as compared to bulk Pt.

Contents

Abstract 1

Introduction 2

Intensity Effects in Bragg Brentano Geometry 3

- Step 1: Normalizing for the incident x-ray beam intensity I_0 5
- Step 2: Accurately estimating the background 6
  - Step 2A: Sample holder 8
  - Step 2C: Finite sample thickness 14
  - Correcting a pure support for absorption and finite thickness 15
- Step 3: Analysis with Rietveld Refinement 16
  - Step 3A: Beam Spill 16
  - Step 3B: Lorentz-Polarization 19
  - Step 3C: Microabsorption and Surface Roughness 20

Modifying the standard XRD experiment 24

Errors in analysis 24
Case Study: 4.8% Pt / amorphous silica 25
STEM 26
XRD 27
Surface oxide phase 30
Lattice Parameter 31
Size and extent of surface oxidation 33
XAS 34
Discussion 35
Applications of the method 35
Limitations of the method 36
Conclusion 38
Acknowledgements 38
Supporting Information 38
References 39

Introduction

Ultra-small (<2nm) supported metal or metal oxide nanoparticles can now be routinely synthesized (Wong, et al. [1]). Supported particles below about 4 nm in size often exhibit interesting chemical properties such as a dramatic dependence of catalytic activity on particle size (Miller, et al. [2]). As particle sizes approach 1 nm, their dispersion (percent of surface atoms) nears 100%, thus allowing efficient catalytic reactions where all atoms can participate. However, systems with such small nanoparticles are difficult to characterize. It is commonly believed that nano crystallites less than 3 nm in size cannot be characterized with workhorse benchtop x-ray diffraction (XRD) instruments; typical reasons cited include low signal to noise and difficulty in separating the diffraction peaks from the background. As one example, Gallagher, et al. [3] reported that synchrotron radiation was required to characterize < 2 nm fully reduced nanoparticles; partially oxidized nanoparticles were reported to be unanalyzable. Without benchtop XRD, researchers must rely on alternate methods such as aberration corrected scanning transmission electron microscopy (STEM), x-ray absorption spectroscopy (XAS), and pair distribution function (PDF) analysis. These methods are more expensive and less accessible than benchtop XRD; for example, the latter two methods are typically performed at a synchrotron and thus often require weeks to even months of advance notice before experiments can be performed.

There are several reasons why benchtop XRD should not be dismissed so quickly. The development of solid-state strip detectors (i.e. linear position sensitive detectors) for benchtop

XRD instruments provides an improvement of signal to noise ratio by about two orders of magnitude over scintillation counters. A preliminary work with such an instrument demonstrated benchtop XRD characterization of 1.2 – 1.6 nm silica-supported gold particles at loadings as low as 0.33 wt% (O'Connell and Regalbuto [4]). Theoretically, the very smallest crystallites will give detectable signals. *Bazin, et al.* [5] numerically simulated the x-ray diffraction patterns from different sized platinum face-centered-cubic (FCC) and body-centered-cubic (BCC) nanoclusters. Their simulations used the Debye scattering equation with calculated atomic scattering factors from *Cromer and Liberman* [6, 7] and were simplified by assuming kinematic scattering only with no thermal disorder. The results showed that even nanoclusters as small as 9 to 13 atoms will give a coherent signal, though the peaks are so broad that many of the individual peaks blend together. These results are consistent with the calculations of *Gallezot, et al.* [8] for electron diffraction of Pd, where nanoclusters as small as 6 atoms provided a recognizable signal. Indeed, zeolite-supported 13-atom Pd clusters were experimentally characterized by *Vogel, et al.* [9] using XRD with Debye Function Analysis (DFA) even without a solid-sate detector, and model particles as small as 13 atoms were routinely used in the DFA analysis of Pt and Ru nanoparticles (*Gnutzmann and Vogel* [10, 11-12]).

The purpose of this paper is to demonstrate the extension of benchtop powder XRD characterization to ultra-small nanoparticles using Rietveld refinement. With this goal in mind, this work presents the extra details that must be considered when characterizing ultra-small crystallites with powder XRD. Relevant intensity effects and their corrections for Bragg-Brentano diffraction are discussed, along with instructions for how the corrections can be implemented using Microsoft Excel and Topas[13]. Details for sample preparation are provided. A robust method is presented for subtracting the background from a supported nanocrystalline sample; this method is based on correcting an experimentally measured diffractogram of the support for differences in intensity effects between it and the nanoparticle containing sample. Finally, a case study of 4.8 wt% Pt / silica (volume weighted size average = 1.3 nm by scanning transmission electron microscopy, STEM) is examined under ambient conditions and analyzed with Rietveld methods. It will be shown that, contrary to the reports of Gallagher, et al. [3], benchtop XRD is capable of characterizing nanoparticles smaller than 2 nm with Rietveld refinement, even when the nanoparticles are partially oxidized under ambient conditions and consist of individual crystal domains with dimensions less than 1 nm in size. These results are corroborated with STEM and XAS.

Intensity Effects in Bragg Brentano Geometry

As XRD peaks broaden, intensity effects that affect the x-ray flux scattered by the sample become more relevant. Even for highly symmetric FCC structures with few peaks, as crystallite sizes approach 1 nm and below the diffraction peaks blend together due to broadening and cease to provide useful information on their own. For less symmetric structures and/or samples with multiple phases the blending of peaks occurs at larger crystallite sizes. When individual peaks are no longer distinguishable, meaningful fits must be done against the entire diffractogram. Any effect that influences the relative intensities of the peaks will change the shape of the entire diffractogram. This is also true for the diffractograms of amorphous materials. For this reason, an

accurate description of the nano-scale fits must account for all intensity effects that impact the diffractogram. Furthermore, if these intensity effects are angle-dependent, then they must be accounted for on a point-by-point basis (each point of the calculated fit adjusted independently). The reason for this is as follows: broad peaks acted upon by an intensity effect that changes significantly over the domain of the peak will be shifted towards the side where the intensity effect is the strongest. We hereafter refer to such peak shifting due to angle-dependent intensity effects as "peak-pulling." A graphical example of the most extreme angle-dependent intensity effect is provided later in the Step 3B: Lorentz-Polarization subsection of Step 3 (Figure 10).

Since intensity factors are so important for the analysis of samples with small crystallites, this work discusses the major contributing intensity effects that affect the diffraction patterns of ultra-small crystallites and presents how these effects can be accounted for. Table 1 lists the intensity effects discussed in this work together with the relative extent of peak-pulling that may be caused when the effects are angle dependent. For clarity, these effects are separated into two categories: sample effects and instrument effects. Sample effects are caused by physical effects related to the sample, while instrument effects are caused by the XRD instrument hardware. In some cases, this categorization is somewhat arbitrary (for example, beam spill results from both sample and instrument effects). However, the classification is especially useful when comparing samples. Except for the x-ray source intensity that may change over time, instrument effects are constant between samples provided that the instrument geometry (and sample holder) is not changed. In contrast, sample effects will vary from sample to sample.

In the following sections, the intensity effects will be discussed in the order that they must be addressed when analyzing XRD data, which matches the order shown in Table 1. The analysis takes place in three main steps. First, all diffractograms are normalized to an external standard. Second, the background of the nano-crystal diffractogram must be identified and separated. Third, the isolated nanocrystalline sample is analyzed with Rietveld refinement.

Table 1. XRD intensity effects discussed in this work.

Step	Intensity effect	Angle	Peak Pull [° 2θ]
1	X-ray source tube	Sometimes*	Negligible
2A	Sample holder (sample-independent)	Yes	N/A
2A	Sample holder (sample-dependent)	Yes	N/A
2B	Absorption	No	N/A
2C	Finite sample thickness	Yes	- 0.10°
3C	Beam spill	Yes	+ 0.30°
3B	Lorentz-Polarization	Yes	- 1.06°
3C	Surface microabsorption (surface roughness)	Yes	+ 0.3°

Sample effects are tabulated in the shaded rows; instrument effects are unshaded. The peak pull is calculated for a Pt (111) peak (Cu K-α) with size broadening corresponding to a 0.87 nm domain size. A negative value indicates an apparent shift to lower angles.
*Depends on how quickly the source intensity changes. If the source intensity changes significantly during a single XRD scan, then the effect on the diffractogram will be angle dependent.

Step 1: Normalizing for the incident x-ray beam intensity I_0

The first intensity effect to account for is the incident x-ray beam intensity I_0. The diffractogram signal that reaches the detector is directly proportional on the flux of x-rays emitted by the x-ray source. As such, variations in I_0 should be corrected by normalizing the entire diffractogram to a standard value – of the intensity effects discussed in this work it is the *only* one that is corrected by normalizing the entire diffractogram. Uncorrected variations in I_0 can lead to serious and irrecoverable errors in the background subtraction and analysis since it becomes impossible to separate I_0-caused changes affecting the entire diffractogram from other intensity changes which impact only portions of the diffractogram (see step 2 below). A good way to gauge I_0 is to measure an intense peak of a solid reference material – we use the (1 0 4) reflection of a NIST 1976c corundum intensity standard custom mounted in an aluminum sample holder. The benefit of a solid reference is that it eliminates variability from sample preparation. If I_0 is observed to change between samples, then each diffractogram should be normalized to the intensity of the solid reference material measured immediately before or after the diffractogram and *not* to some "common point" between diffractograms. Readers should also note that normalizing their diffractograms will require corrections to the statistical experimental uncertainties (see the "Statistical Errors" section in the supplementary information for more information).

Different instruments will exhibit different degrees of intensity drift. It is up to XRD users to know their instruments and to determine if changes in I_0 are significant to their experiments. We offer the following information to aid XRD users in making their decisions: for supported nanoparticle samples *any* observable change in I_0 may be significant – especially if the nanoparticles' contribution to the diffractogram is low compared to that of the support (e.g. low weight loadings). Instruments may be especially vulnerable to changes in I_0 under the following conditions:

- Non-constant source / detector temperature
- Weeks to months between measurements (x-ray sources can degrade over time)
- Changes to the instrument hardware

For the Rigaku Miniflex II benchtop XRD used in this work, the emitted x-rays can show a significant drift in I_0 over time ranges on the order of a single diffractogram measurement (Figure 1). The main source of this drift is believed to be the varying temperature of the cooling water used to cool the x-ray tube (our instrument uses a closed-loop chiller which does not include temperature control). As the cooling water changes temperature the x-ray tube temperature also changes; this is believed to cause the observed change in intensity. The fact that this instrument's I_0 can significantly change over the course of a single experiment necessitates special experimental consideration: fast scan speeds to minimize differences in I_0 between the beginning and ending of each scan, multiple scans to improve resolution, and measurement of an intensity standard at the beginning and ending of each scan.

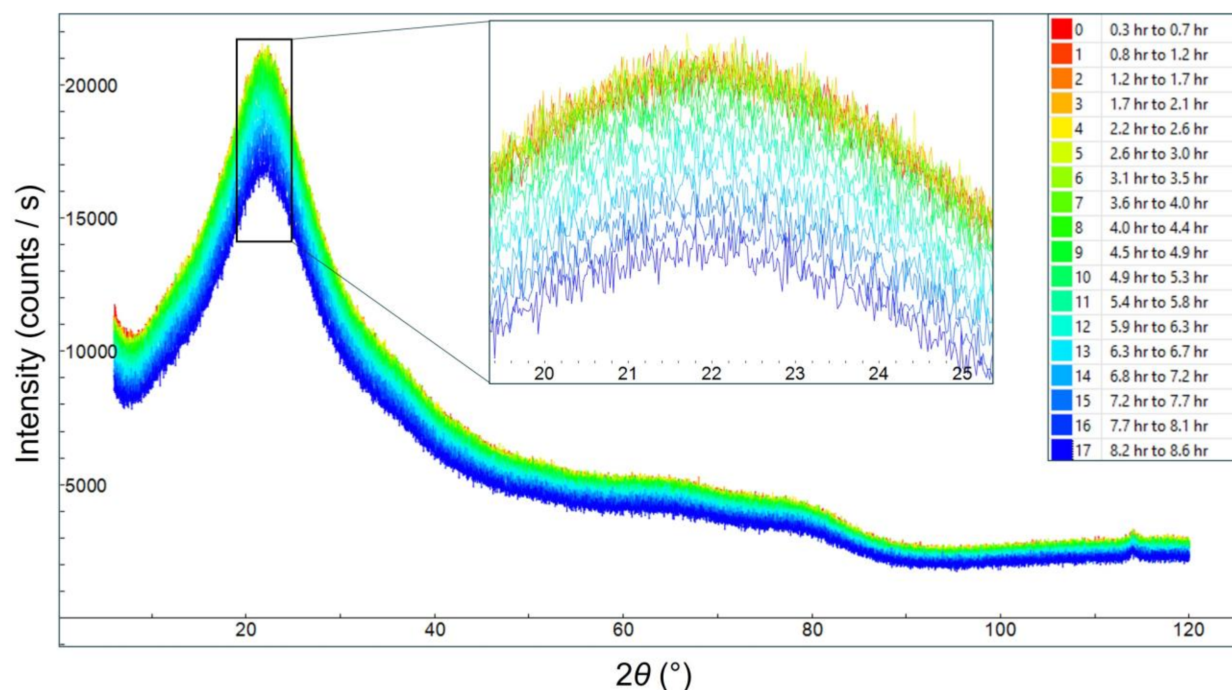

Figure 1. Example of x-ray source intensity drift over time. The back-to-back diffractograms display a slow increase in intensity for the first five runs; the remaining runs exhibit a more rapid decrease in intensity. Intensity is given in counts per dwell time (τ).

Figure 2 (A) depicts the result after adjusting for drift and averaging multiple runs together for a series of Au samples supported on silica. It is important to note that after properly adjusting for changes in I_0 other intensity effects become evident. Figure 2 (A) shows that after correcting for I_0 the silica peaks (near $2\theta = 22°$) still have significantly different intensities. These differences are due to other angle-dependent effects. Herein all diffractograms were first corrected for intensity drift against the (1 0 4) reflection of a NIST 1976c intensity standard. For the interested reader, additional information on the incident x-ray intensity and how it can be accounted for is provided in the supplementary information.

Step 2: Accurately estimating the background

After normalizing I_0 for all samples using an intensity standard, the coherent scattering of the nano-crystals must be isolated. This is done by comparing the supported nanoparticle sample's diffractogram to that of the pure support. However, unknowing researchers often do this incorrectly – e.g. by normalizing the entire support diffractogram to that of the nanoparticle diffractogram. The correct procedure for comparing diffractograms requires knowledge of the components that make up a diffractogram and is illustrated for a series of silica-supported gold samples in Figure 2:

1. For each of the samples to be compared, the portion of the diffractogram corresponding to the contribution of the sample holder must first be identified (Figure 2A). The process is discussed in-depth below, see "Step 2A: Sample holder." We note that in Figure 2A all samples were measured using the same sample holder and the sample holder contribution is assumed constant between samples.

2. Once identified, the sample holder contribution to the diffractogram is subtracted (Figure 2B). The remaining counts of each diffractogram come strictly from the sample and are composed of the scattering from the nanoparticles and support.
3. Physical differences between the isolated sample diffractograms are accounted for by taking two sample effects into account (Figure 2C). The first effect is the absorption of x-rays by the samples (see “Step 2B: Absorption”). The second effect is the finite thickness of the samples (see “Step 2C: Finite sample thickness”). These two effects are related to one another and must be accounted for together, along with any differences between the total volume of the samples (see “Correcting a pure support for absorption and finite thickness”).
4. The necessity for this last step is dependent on how the user accounts for statistical errors during their analysis. Once the diffractograms have been adjusted for absorption and finite thickness, the sample holder contribution may be added back to each diffractogram (Figure 2D). In Topas, this step is necessary if the user wants to use Topas’ default error statistics (which are valid if the data is in total counts and has not been adjusted). If the user adjusts their data (e.g. by normalizing to an intensity standard) the counting statistics are changed and the default is no longer valid. In this case the user can calculate the new errors and import them into Topas as an .xye file, making it unnecessary to add back the sample holder contribution. See the “Discussion of Errors” in the SI for more details, including information on updates that are required for some commercial users of Topas to be able to import error information via .xye files.

Figure 2D shows that once corrected, the intensity and width of the main amorphous silica peak (22° 2θ) for all the samples are in close agreement. The diffractograms of the pure treated supports now provide a clear baseline above which gold peaks of increasing weight loading can clearly be seen (inset of Figure 2C). This baseline is the “background” to be used during (or subtracted prior to) the analysis in Topas.

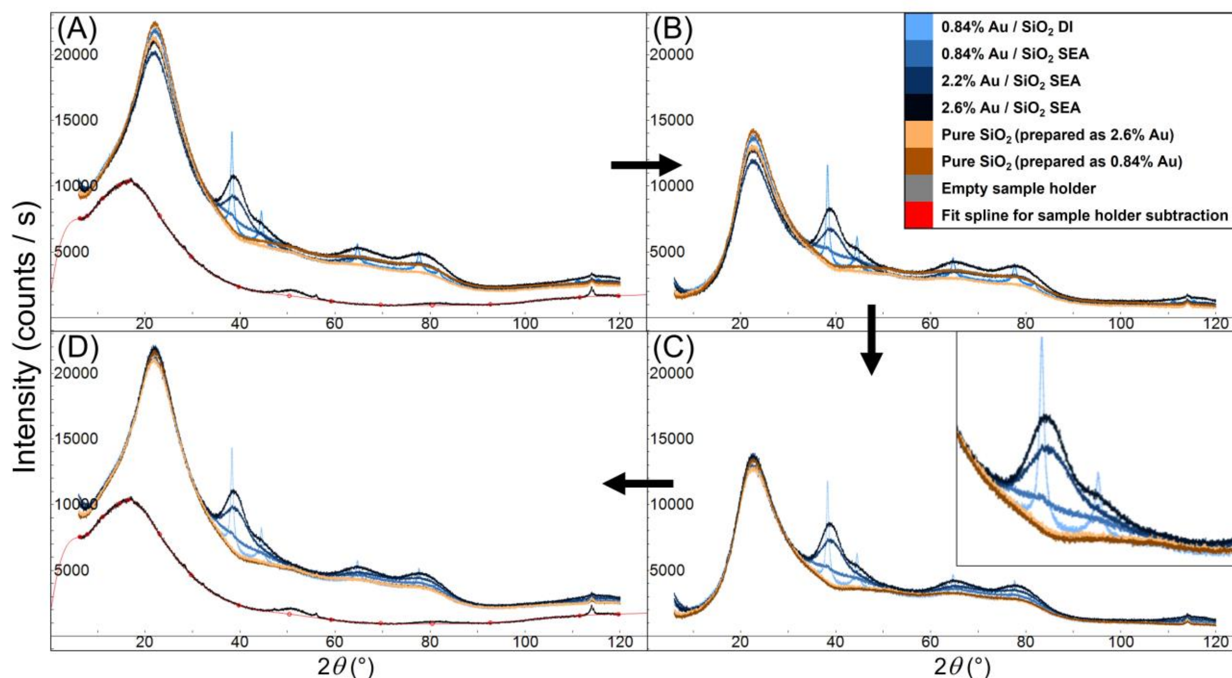

Figure 2. A series of Au / silica (Aerosil 300) samples demonstrating the effectiveness of accounting for sample mass, x-ray mass attenuation, and finite thickness intensity factors. Samples were prepared with either dry impregnation (DI) or strong electrostatic adsorption (SEA). (A) Data normalized to a common source intensity. Each diffractogram is the average of six runs taken at 5° min^{-1}. (B) Diffractograms after subtracting the background (fit spline). (C) Background-subtracted diffractograms after correcting for differences in x-ray absorption and finite sample thickness. (D) Corrected diffractograms with the background added back (in preparation for Rietveld analysis). (Peaks in the sample holder at 53°, 82°, and 114° are from the portion of the sample holder covered by the sample; the spline is manually fit to reduce the maximum possible error at these points. See the following section and supplementary information for more details.)

Step 2A: Sample holder

The sample holder can contribute both sample dependent scattering and sample-independent scattering to a diffractogram. Accurate background subtraction relies on quantifying these contributions. The extent of the contributions will depend on the instrument hardware and sample holder dimensions. For the Rigaku Miniflex II and silicon sample holder used for this work, there is a significant sample-independent contribution to each diffractogram, and a smaller sample-dependent contribution (Figure 3). The reason for this can be seen in Figure 4 where the x-ray beam is shown covering a large portion of the silicon mirror that surrounds the sample cavity. This single crystal of silicon is cut at a low index plane to remove sharp peaks from appearing in the diffractogram. We propose that the surface of the silicon is oxidized and gives a diffuse silica bump that is skewed in shape and position by the different amounts that are illuminated by the XRD beam at varying incident angles. The diffractogram contribution coming from the surface of the mirror will be constant for all samples. Figure 3 shows that for our instrument geometry and sample holder this constant contribution (that includes the primary beam scatter from the x-ray source onto the detector, shown in red) from the sample holder can be quite significant (black). The sample-dependent contribution (grey) comes from the silicon/silica at the bottom of the cavity; this contribution is greatest when there is no sample in the holder and decreases when it is covered by sample. The contribution will be zero when covered by a sample that absorbs all the x-rays.

The sample holder contributions can be determined by measuring a series of diffractograms. The diffractogram of the empty sample holder provides the combined sample-independent contribution and maximum possible sample-dependent contribution (sum of the red, black, and grey shaded regions in Figure 3). The sample-independent region is obtained by filling the sample cavity with a highly absorbing sample that completely shields the bottom of the sample holder from the x-rays. This sample must be highly crystalline so that the diffracted peaks can be separated from the sample holder contribution (see the supplementary information for a discussion on how to determine if a sample will function as a highly crystalline reference). The diffractogram of the sample holder filled with the highly absorbing sample is then processed to separate and remove the sample's peaks from the baseline; once isolated the resulting baseline corresponds to the sample-independent holder contribution (sum of the red and black shaded regions in Figure 3). By subtracting the sample-independent contribution from the empty sample holder contribution, the sample-dependent region of the sample holder is obtained. To identify the most accurate estimate of the sample-dependent contribution, a third highly crystalline sample could be made that would have the same x-ray mass attenuation as the sample to be corrected for sample effects. This could be achieved by mixing a lightly x-ray absorbing sample with a heavily x-ray absorbing sample, as long as both samples are highly crystalline.

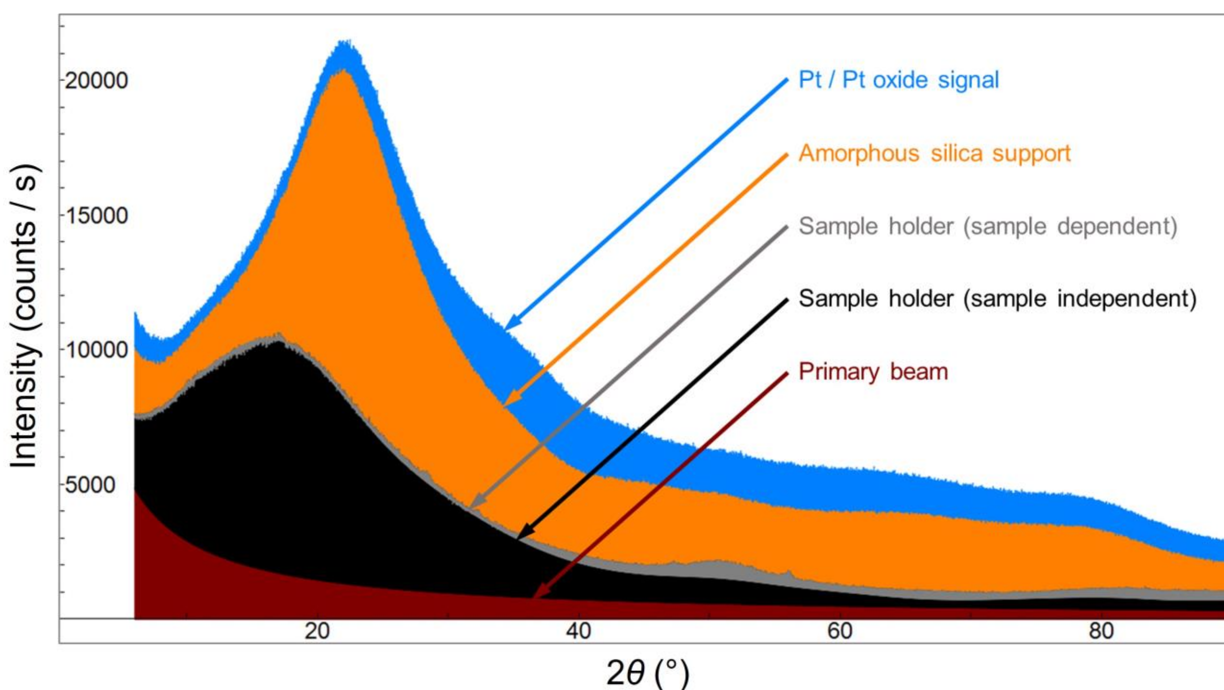

Figure 3. 4.8% Pt / silica (Aerosil 300) diffractogram components. Except for the primary beam scatter (red), all the portions of the diffractogram were obtained by separate diffraction measurements, with adjustments for drift and sample intensity effects. The intensity of the primary beam scatter has been arbitrarily chosen and displayed to remind the readers that the sample independent sample holder diffractogram contains the primary beam scatter, therefore changing the atmosphere through with the x-ray beam travels (for example in an in-situ measurement) may also have an effect on the diffractogram.

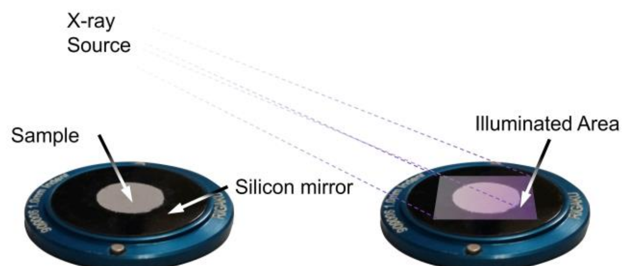

Figure 4. Irradiation of a "zero background" sample holder in the Rigaku Miniflex II.

The reason why it is so important to identify the sample holder's diffractogram contribution is that it must be subtracted from the diffractogram *before* the sample effects (absorption, finite thickness, and total volume) can be corrected. The sample-independent contribution from the sample holder depends only on the incident beam intensity, the sample holder itself, and the atmosphere inside the diffractometer. It does not depend on the sample in the holder, so including it in the adjustment for sample effects will introduce errors. These errors will be especially prominent if the sample holder contribution contributes a significant portion of the entire diffractogram (as is the case in Figure 3). The sample-dependent contribution from the sample holder will be affected by the differences between samples, but not in the same way as the sample itself. For this reason, it should also be subtracted before the sample effects are corrected.

Step 2B: Absorption

The attenuation of x-rays as they travel through a sample (also known as x-ray mass absorption) is related to the linear absorption coefficient μ [cm^{-1}], or $\bar{\mu}$ (the average coefficient for a combination of elements). Figure 5 shows three samples containing equal amounts of amorphous silica, but physically mixed with different ratios of two crystalline powders: quartz (SiO_2) and tin (Sn). The sample mixed only with quartz has the lowest $\bar{\mu}$ (11.7 cm^{-1}) and therefore the most intense amorphous silica diffractogram (see the broad peak centered around 21° 2θ). The sample mixed only with tin has the highest $\bar{\mu}$ (17.8 cm^{-1}) and therefore significantly lower intensity of the amorphous silica. Figure 6 shows the x-ray mass attenuation coefficients (μ / ρ [cm^2 g^{-1}]; ρ is the density of the sample) by element for Cu K-α radiation; the silicon and oxygen present in quartz have much lower mass attenuation coefficients than that of tin. The physical significance of the mass attenuation coefficient is that x-rays will not penetrate elements with higher coefficients as easily as they do elements with lower coefficients. As x-rays travel through the samples of Figure 5, less x-rays pass through the tin than through the quartz. Fewer x-rays are therefore available to scatter from the silica in the tin-containing sample than in the quartz-containing sample, and the ultimate result is that the silica diffractogram is less intense in the tin-containing sample.

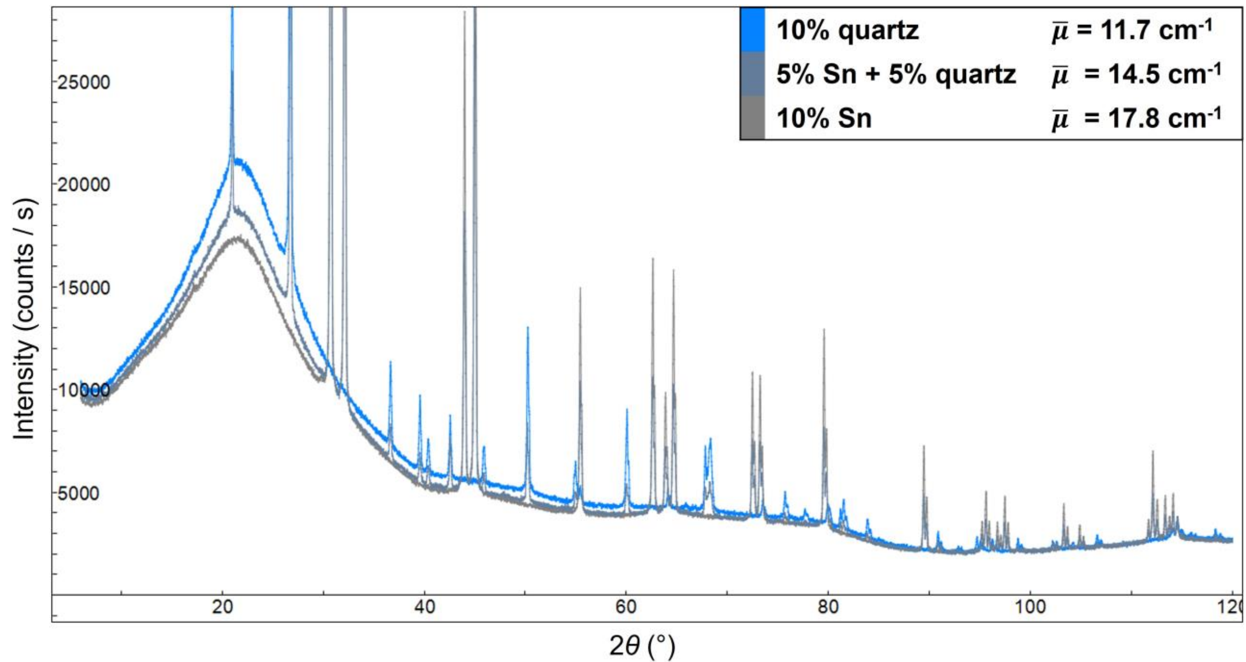

Figure 5. Demonstrating the effect of different amounts of microabsorption on equal loadings of amorphous silica.

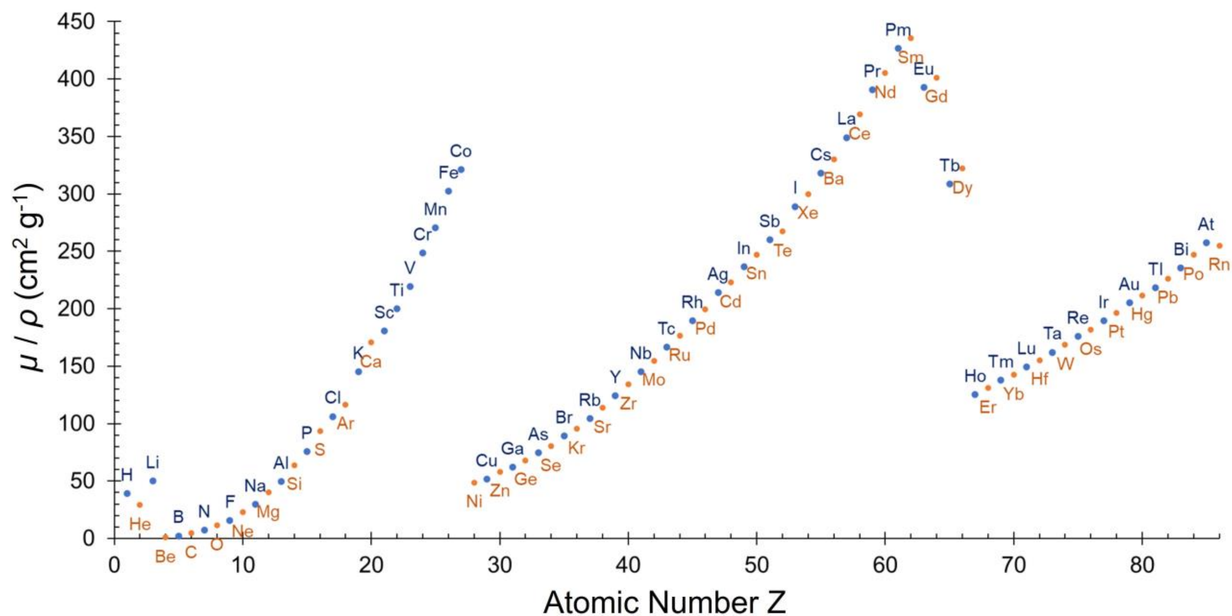

Figure 6. X-ray mass attenuation coefficients by element for copper K-α radiation (1.5406 Angstrom). Derived from linear interpolation of NIST data (Table 3 of Ref. [14]). Alternating colors are used to clarify the labeling, where needed.

It is critical to account for absorption in samples with supported nano-crystallites, both for identifying the "background" in the nano-crystallite containing sample and for fitting crystal structures with Rietveld refinement. For a supported nano-crystallite sample, the "background" is obtained by separately measuring the pure support. Any difference in absorption between the sample and its support will cause differences between the measured support and the actual support's contribution to the nano-crystallite sample's diffractogram. This is why for many

samples the pure support often appears to give a more intense diffractogram than the nanoparticle containing support. For Rietveld refinement, the absorption will cause discrepancies between the calculated diffractograms and experimental data unless it is accounted for.

X-ray mass attenuation coefficients μ / ρ for elements with atomic numbers 1 through 92 can be obtained from Table 3 of Hubbel and Seltzer [14]. The data is presented by element as a function of wavelength. For compounds and mixtures, μ / ρ values are obtained by adding together the x-ray mass attenuation coefficient of each element present in the mixture multiplied by the element's mass fraction w_i:

$$\frac{\mu}{\rho} = \sum w_i \times \left(\frac{\mu}{\rho}\right)_i . \qquad \text{Equation 1}$$

To obtain the linear mass absorption coefficient μ, the mass attenuation coefficient must be multiplied by the sample's density ρ. For powder samples, the density depends on the volume of the spaces between particles (i.e. packing density). Knowledge of both the sample mass and volume are thus required; therefore, the dimensions of the sample holder must be carefully measured along with the mass of each sample. Also note that the calculation requires knowledge of the mass fractions of each element present; this information is best obtained with a separate characterization technique, e.g. by inductively coupled plasma - optical emission spectroscopy (ICP-OES) or x-ray fluorescence (XRF). It can quickly become tedious to calculate μ for mixtures containing multiple elements; a tool is provided in the supplementary information to aid in the calculation.

According to Hermann and Ermrich [15], absorption in fine multi-phase powders can be corrected as follows:

$$\frac{I_i'}{I_0} = \frac{\alpha_i[1-2(\mu_i-\bar{\mu})b_i]}{2\bar{\mu}} . \qquad \text{Equation 2}$$

In this description, I_i' is the intensity reflected from phase i, I_0 is the incident beam intensity, α_i is the volume fraction of phase i, μ_i is the x-ray mass attenuation coefficient of phase i, $\bar{\mu}$ is the mean x-ray mass attenuation coefficient of the entire powder sample, and b_i is defined as

$$b_i = \frac{2B_i}{3}, \qquad \text{Equation 3}$$

where B_i is the mean breadth of the particles of phase i. In Equation 2, the $(\mu_i - \bar{\mu})b_i$ term represents the contribution of bulk microabsorption (surface microabsorption is neglected). Microabsorption is discussed in detail later. It is difficult to correct for since corrections discussed in the literature either require knowledge of both the powder particle sizes and detailed knowledge of how the powder volume fraction varies with depth, or refine parameters related to these physical variables. For comparing a sample and its support, the best approach is to reduce the effects of microabsorption as much as possible: firstly by finely grinding the samples and secondly by making the XRD sample surfaces as smooth as possible when loading the samples into the XRD sample holder (see the videos provided in the supplementary information for more information on

sample preparation). For very fine particles with x-ray mass attenuation values close to the sample average, the $(\mu_i - \bar{\mu})b_i$ term becomes negligible and the intensity of the reflection from phase *i* is estimated by

$$I_i' = \frac{I_0 \alpha_i}{2\bar{\mu}}. \quad \text{Equation 4}$$

Zevin, et al. [16] point out that if the $(\mu_i - \bar{\mu})b_i$ term in Equation 2 is not truly negligible, then for low absorbing phases ($\mu_i < \bar{\mu}$) the adjusted intensity will be amplified, while high absorbing phases ($\mu_i > \bar{\mu}$) will be diminished. Brindley [17] classifies powders in terms of the parameter μD, where D is the linear size of a particle (according to Hermann and Ermrich [15], usually the mean chord length $\bar{l}$ is used). In this work, we assume that the parameters D and B are equivalent. Microabsorption is directly related to the value of μD, i.e. μB. Fine particles are defined as having $\mu B < 0.01$; these samples will have negligible microabsorption. In terms of Equation 2 and Equation 3, the goal of sample preparation would therefore be to have $\mu_i B_i < 0.01$. For nano-crystallites, the value of B is so small that this is valid, even when μ is high (e.g. for Au or Pt). For the support, μ tends to be closer to that of the bulk (since the weight loadings of nano-crystallites tend to be low). However, support particle sizes are often large; they can be reduced by grinding the sample before measurement.

The comparison of the intensity of the same phase between two samples 1 and 2 can be written as

$$\frac{I_{i,1}'}{I_{i,2}'} = \frac{\alpha_{i,1}\bar{\mu}_2}{\alpha_{i,2}\bar{\mu}_1}, \quad \text{Equation 5}$$

where $I_{i,1}'$ is the intensity of the reflection from phase *i* in sample 1, and $I_{i,2}'$ is the intensity of the reflection from the same phase *i* in sample 2. It is convenient to write the volume fractions in terms of the individual phase volumes $V_{i,1}$ and $V_{i,2}$ (these are strictly the phase volume and do not include empty space from such things as pores or gaps between particles) and the total sample volumes $V_{T,1}$ and $V_{T,2}$:

$$\frac{I_{i,1}'}{I_{i,2}'} = \frac{V_{i,1}\bar{\mu}_2}{V_{i,2}\bar{\mu}_1}\left(\frac{V_{T,2}}{V_{T,1}}\right). \quad \text{Equation 6}$$

If the density of phase *i* in each of the samples is assumed identical between samples 1 and 2 (note that the density of each phase does not include empty space from pores, interparticle space, etc. and is therefore independent from the powder density), this becomes

$$\frac{I_{i,1}'}{I_{i,2}'} = \frac{m_{i,1}\bar{\mu}_2}{m_{i,2}\bar{\mu}_1}\left(\frac{V_{T,2}}{V_{T,1}}\right), \quad \text{Equation 7}$$

where $m_{i,1}$ and $m_{i,2}$ are the masses of phase *i* present in sample 1 and 2, respectively. One of the most prominent experimental differences of this method as compared with a typical XRD analysis is the requirement to measure the sample mass. Equation 7 is a useful form, since the mass of each phase can be calculated from the measured sample mass if the weight loadings of the sample are already known. The x-ray mass absorption coefficients can be obtained per the discussion of the

previous section. The ratio of the total sample volumes should be close to 1, if the samples are prepared in the same XRD sample holder. However, slight differences in sample prep may cause a need for adjusting this ratio during analysis. One way to minimize the adjustment of this ratio for nanoparticle samples is to keep the mass of the *support* constant between samples while using the same sample holder. Another helpful tip is to prepare the pure support with as close to the same treatment as the nanocrystalline sample as possible: pH treatment, drying method, reduction, etc. This will help produce similar porosities and powder densities between the samples and thus keep the total volume ratio close to 1.

Note the assumptions required in the derivation of Equation 7. Particle sizes must be very fine ($\mu D < 0.01$), so it is good practice to finely grind samples before loading them into the sample holder, especially for samples with high μ. Phase densities must be equivalent between samples, so the pure support should be measured under the same conditions (e.g. temperature and pressure) as the nanoparticle sample. The total volume ratio is difficult to measure; it is best to keep the ratio as close to one as possible by using the same sample holder, similar mass of support, and similar treatment method (e.g. pH treatment, drying, reduction) for the samples.

Step 2C: Finite sample thickness

A normal Bragg-Brentano x-ray diffraction analysis assumes an “infinitely thick” sample, i.e., none of the incident x-rays pass completely through the sample. If x-rays do reach the bottom of the sample holder, there is a reduction from the expected diffraction intensity. This “finite thickness” reduction increases with increasing incident angle, since the x-rays will travel through less sample before reaching the bottom of the holder. Figure 7 compares the correction that must be made for four common catalyst supports: carbon, silica, zirconia, and ceria. The correction depends exponentially on the total x-ray attenuation coefficient of the powder sample. Samples with low μ values such as carbon will need significantly more correction than samples with high μ such as ceria. Figure 7 also shows the effect of placing 5 wt% Pt onto the carbon support. The large difference in x-ray mass attenuation between Pt and C results in the total sample μ increasing from 2 cm^{-1} to 6 cm^{-1}. For such a system a large correction must be made to match the pure support diffractogram to that of the metal containing sample.

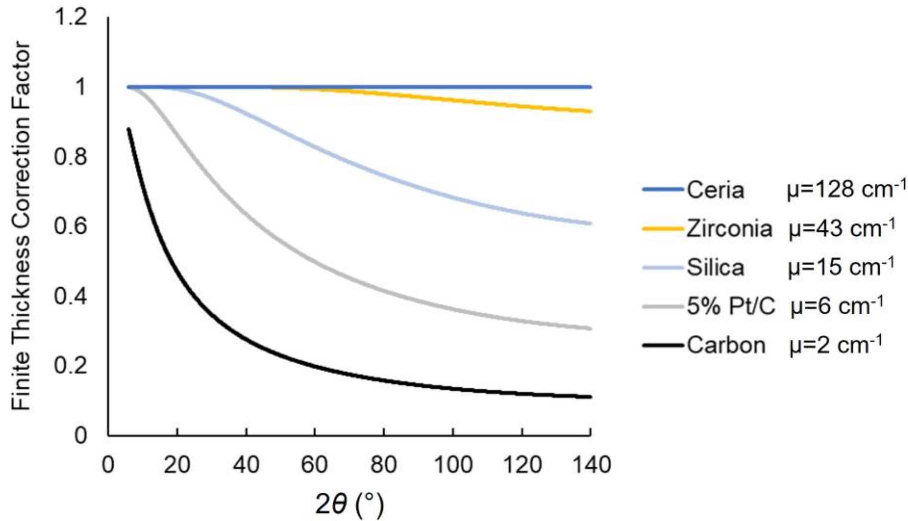

Figure 7. Comparing the finite thickness correction factors of different samples. Calculations assume 10mg of sample in a sample holder cavity 0.288mm deep and 10.21 mm in diameter.

For Bragg-Brentano geometry, Dinnebier, et al. [18] report the correction factor A for finite thickness as

$$A = 1 - \mathrm{e}^{-\bar{\mu} t_s \frac{2}{\sin\theta}}, \qquad \text{Equation 8}$$

where t_s is the thickness of the sample and θ is the incident angle. To compare the intensities of a common phase in two separate samples, one can write

$$\frac{I_{i,1}'}{I_{i,2}'} = \frac{A_1}{A_2}. \qquad \text{Equation 9}$$

Correcting a pure support for absorption and finite thickness

Combining Equation 9 with Equation 7 gives

$$\frac{I_{i,1}'}{I_{i,2}'} = \frac{m_{i,1}\bar{\mu}_2 A_1}{m_{i,2}\bar{\mu}_1 A_2}\left(\frac{V_{T,2}}{V_{T,1}}\right). \qquad \text{Equation 10}$$

If the nano-crystallite containing sample is designated as sample 1 and the pure support as sample 2, then the intensity of the support reflection in the nano-crystallite sample ($I_{i,1}'$) can be obtained from the intensity of the pure support reflection ($I_{i,2}'$) as follows:

$$I_{i,1}' = \frac{I_{i,2}' m_{i,1}\bar{\mu}_2 A_1}{m_{i,2}\bar{\mu}_1 A_2}\left(\frac{V_{T,2}}{V_{T,1}}\right). \qquad \text{Equation 11}$$

$I_{i,2}'$ is obtained by subtracting the sample holder contribution from the pure support's XRD pattern. Once $I_{i,1}'$ has been estimated from $I_{i,2}'$ using Equation 11, the sample holder contribution for the nano-crystalline sample is added to it. The final result is an accurate estimate of the "background" for the nano-crystalline sample.

Step 3: Analysis with Rietveld Refinement

Once the "background" has been obtained by adjusting the pure support to match the sample, it is subtracted from the nanoparticle sample in order to isolate the scattering from the nanoparticles. This is done by subtracting a curve fit to the adjusted support (such as a high-order Chebyshev polynomial); the benefit of subtracting a curve (rather than subtracting the adjusted support diffractogram) is to prevent the statistical errors of the support from being added to those of the nanoparticle sample. The nanoparticle sample (together with calculated statistical errors) is imported as an xye file into Topas (see the "Case Study" below for an example and the supplementary information for details, including notes about a software update that may be required for users of the commercial Topas version). Phases of interest are identified, and their structures imported into Topas. For the actual Rietveld refinement, very little is allowed to refine, since it is easy to "fit an elephant" with such broad peaks. A basic analysis will only allow the overall scale factor and crystallite size for each phase to refine (see the supplementary information "notes on peak broadening" section for a brief discussion of peak broadening). All other parameters (emission profile, instrument profile, correction factors, etc.) are measured or calculated prior to the refinement and are fixed. Once the most promising fits are identified, the metal lattice parameter (if a metallic phase is present) and two surface roughness parameters may be allowed to refine in order to account for any surface roughness that may be present in the sample. It is important to note that all intensity corrections should be made on a point-by-point basis rather than Topas' default of scaling entire peaks by the value of the intensity factor at the peak's center. See the supplementary info for detailed information on what modifications need to be made to the Topas macros in order to scale for the intensity factors on a point-by-point basis. In addition to the intensity factors already discussed, there are three remaining intensity factors that come into play only during the Rietveld refinement: beam spill, Lorentz polarization, and surface roughness. The following sections discuss these intensity factors in more detail.

Step 3A: Beam Spill

The calculation of a diffraction pattern from a structure assumes that the intensity of the incident x-rays striking the sample is constant. Beam spill is a physical effect related to the x-ray beam divergence and incident angle on the sample; at low angles the beam spreads over a wide area while at high angles the beam covers a much smaller area. Beam spill (also known as overspill) occurs when the region illuminated by the x-ray beam on the plane containing the sample extends outside of the sample. Figure 8 compares the beam spill vs. incident angle for two separate instrument geometries using the same sample holder. Geometry (A) has much greater beam spill than geometry (B). It is tempting to think that this means geometry (B) is more desirable. However, the benefit of using a wider x-ray beam is that more x-rays strike the sample at higher angles, giving a stronger signal to noise ratio (e.g., comparing the instrument geometries of Figure 9 at 30° reveals a greater area of the sample struck by x-rays for geometry A). This increased signal from a wider x-ray beam at high angles is desirable - if the decreased low-angle intensities caused by beam spill can be corrected for. This argument also applies (though to a lesser extent) to instruments where variable incident slit widths can be used to control the play of the x-ray beam. For users trying to decide whether to use the variable slit option, we also note that Dinnebier, et al. [18] recommend against using variable slits for Rietveld refinement due to several reasons

including imprecisions in slit openings and decreasing resolution at increasing 2θ. Diffraction profiles obtained with variable slits will also require a correction function that needs to be implemented on a point-by-point basis.

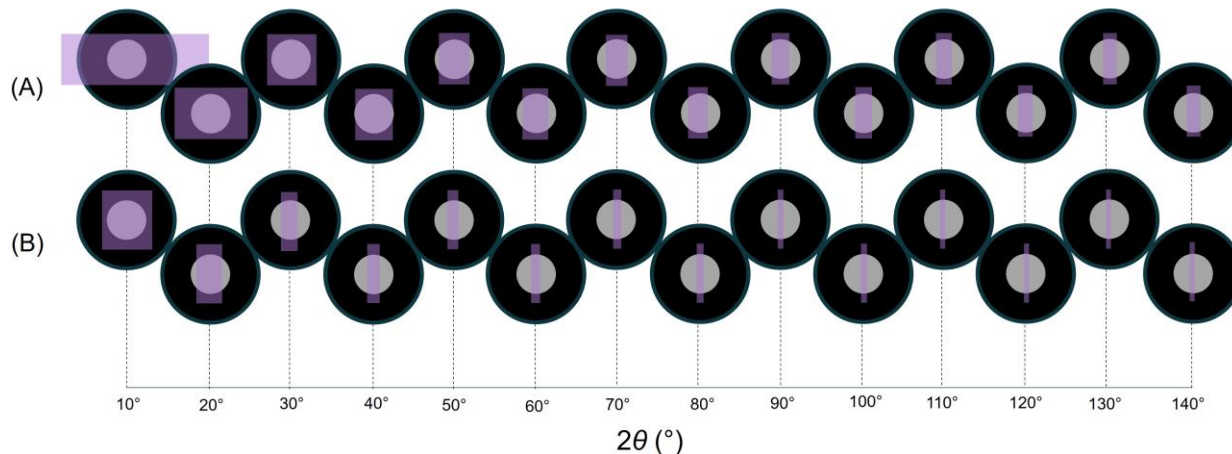

Figure 8. Comparing beam spill vs. incident angle for two instrument geometries: (A) Goniometer radius = 150mm, divergence slit = 1.25° (2θ); (B) Goniometer radius = 217.5mm, divergence slit = 0.3° (2θ). The purple shaded region is the total illuminated area of the beam, the sample is depicted by the inner grey circles.

By default, Topas implements a one-dimensional correction for beam spill. This assumption assumes a constant sample length (S) equivalent to the diameter of the sample. Dinnebier, et al. [18] present the correction factor (Ov) as

$$Ov = \frac{S}{L_D}, \qquad \text{Equation 12}$$

where L_D is the irradiated length of the beam in the plane of the sample, approximated by

$$L_D = \frac{R\varphi}{\sin\theta}. \qquad \text{Equation 13}$$

Here, R is the goniometer radius, φ is the divergence slit opening in radians, and θ is the incident angle. This beam spill correction is implemented only at lower angles while L_D is larger than the sample length; at higher angles the correction factor is given a value of 1.

For diffraction patterns with sharp peaks the one-dimensional correction is a useful tool, but diffraction patterns with nano-crystallite containing samples require greater accuracy. A two-dimensional correction is needed, where the curvature of the sample with respect to the beam is taken into account. It is also helpful to take any sample displacement into account, since a vertical offset will change the play of the beam over the surface. We start by defining our 2-D correction factor Ov_{2D} as

$$Ov_{2D} = \frac{S_{2D}}{A_{2D}}, \qquad \text{Equation 14}$$

where S_{2D} is the irradiated sample area and A_{2D} is the total area in the plane of the sample that is irradiated by the incident x-ray beam. A_{2D} can be written as

$$A_{2D} = Axial\ beam\ width \times (s_1{}' + s_2{}'), \qquad \text{Equation 15}$$

where s_1' and s_2' are the equatorial irradiated lengths on the primary and secondary sides of the sample center, respectively, as shown in Figure 9 (A). The axial beam width depends on the goniometer radius R and the primary Soller slit angle SS:

$$Axial\ beam\ width = 2R\tan\left(\frac{SS}{2}\right). \qquad \text{Equation 16}$$

Expressions for s_1' and s_2' in terms of the incident angle θ and height displacement h are derived trigonometrically (see the supplementary info for the derivation):

$$s_1' = \frac{R\sin\left(\varphi/2\right)}{\sin\left(\theta+\varphi/2\right)} + \frac{h}{\tan\left(\theta+\varphi/2\right)}, \qquad \text{Equation 17}$$

$$s_2' = \frac{R\sin\left(\varphi/2\right)}{\sin\left(\theta-\varphi/2\right)} - \frac{h}{\tan\left(\theta-\varphi/2\right)}, \qquad \text{Equation 18}$$

where ϕ is the total angular opening of the divergence slit. An expression for S_{2D} can be obtained with either trigonometric arguments or calculus (see the supplementary info for the derivation):

$$S_{2D} = d^2\sin^{-1}\left(\frac{s_{m1}}{d}\right) + s_{m1}\sqrt{d^2 - s_{m1}{}^2} + d^2\sin^{-1}\left(\frac{s_{m2}}{d}\right) + s_{m2}\sqrt{d^2 - s_{m2}{}^2}. \qquad \text{Equation 19}$$

In this equation, d is the sample radius, s_{m1} is the minimum of s_1 and d, and s_{m2} is the minimum of s_2 and d. The reason for expressing the equation this way is so that the equation can be more easily expressed in Topas' programming language. See the supplementary information for the code used to update the beam spill approximation from a 1-D correction to a 2-D correction. Figure 9 (B) compares the 1D beam spill correction to the 2D beam spill correction and to the 2D beam spill correction with an extensive height error. Accounting for the 2-dimensional curvature of the sample makes a large difference, especially if the sample diameter is small. Height error (sample displacement) has little effect on beam spill.

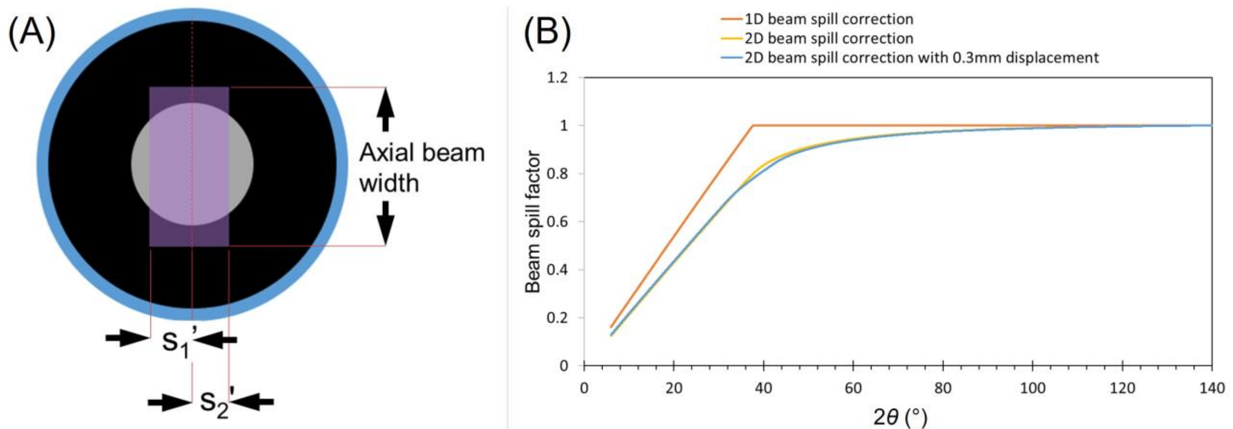

Figure 9. (A) X-ray beam in the plane of the sample, separated into the primary region bordered by s1 and the secondary region bordered by s2. (B) 1D and 2D correction factors for a sample diameter of 10.16 mm. Note that in this figure the 2D correction factors are normalized to their maximum value for better comparison with the linear correction.

Step 3B: Lorentz-Polarization

The Lorentz-polarization correction is an angle-dependent correction factor that accounts for two geometric effects (the Lorentz factor) as well as the polarization of the x-ray beam after scattering. It has been well documented, and for a detailed understanding of its physical basis this work will defer to the excellent discussions of other authors, such as Dinnebier, et al. [18] and Pecharsky and Zavalij [19]. The latter writes the correction factor for powder diffraction with no monochromator as

$$LP = \frac{1+\cos^2 2\theta}{\cos\theta \sin^2\theta}. \quad \text{Equation 20}$$

Figure 10 (A) shows how significant the Lorentz-polarization factor is. Low angle peaks are greatly amplified with respect to the higher angle peaks. The default implementation of the correction factor in Topas scales each calculated peak by the LP value at the peak center. This may be fine for sharp peaks, but it can lead to significant errors with broad peaks. Figure 10 (B) shows the difference between a peak scaled to the Lorentz-Polarization factor only by its center value (orange) vs. a peak scaled on a point by point basis (every calculated point scaled independently). The result of scaling on a point by point basis is an apparent peak shift toward lower angles where the Lorentz-Polarization factor is more intense (peak pulling). The extent of this shift depends on how much the LP factor changes between the left and right peak edges and can be more than 1° 2θ. The shift is observed experimentally and will be larger for peaks at low angles and less for peaks at high angles (up to around 100° 2θ, where the LP correction reaches a minimum and begins to increase again – the corresponding peak pulling at angles > 100° 2 theta is to higher angles). The peak pulling effect of Lorentz-Polarization explains why broad experimental peaks below 100° 2θ appear shifted to lower angles – a fact which if not accounted for properly can lead to false analyses claiming increased lattice constants. A similar apparent peak shift due to broad peaks being multiplied by an angle-dependent intensity factor is discussed in Gallezot, et al. [8], where the intensity factor is the angle-dependent atomic form factor (see *Limitations of the method*).

It is important to note that any angle-dependent intensity factor must also be accounted for on a point-by point basis. For example, scaling a peak for beam spill will shift peaks to the right (see Figure 9 B) while peaks scaled for finite thickness (Figure 7) will shift peaks to the left. See the supplementary info for a discussion on user macros that can be applied / modified in Topas in order to implement the point-by-point scaling of intensities.

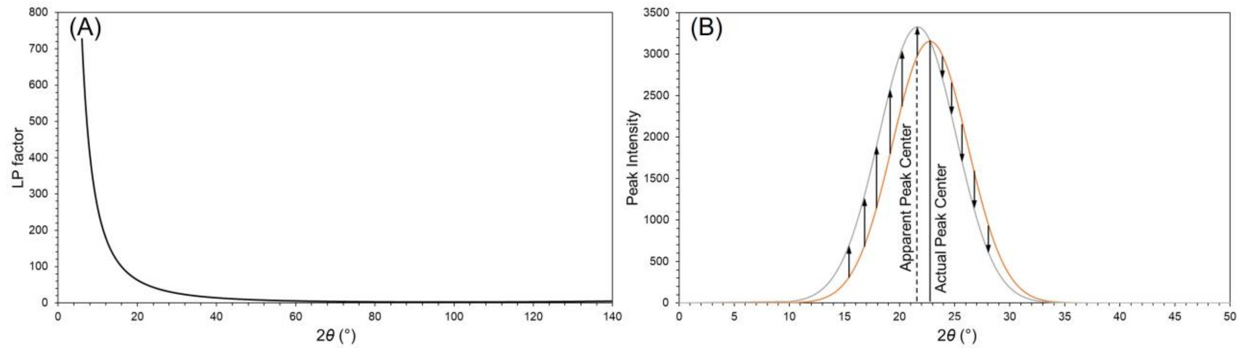

Figure 10. (A) Lorentz polarization correction factor for unpolarized (no monochromator) radiation. (B) Scaling point-by-point (black) vs. scaling by peak center (orange) with Lorentz-Polarization: apparent peak shift for broad peaks (peak pulling). The featured peak corresponds to a crystallite size of 1.1nm

Step 3C: Microabsorption and Surface Roughness

Surface roughness – as the name suggests – comes from a sample surface that is not perfectly smooth. Figure 11 shows how the volume fraction of powder samples increase from zero at the surface to the bulk volume fraction at a certain depth. A surface is considered smooth if the transition is sudden (as a function of depth). For a rough surface, the transition is more gradual. The observed effect of surface roughness is a decrease in intensity at low angles. The effect can be quite significant: Pitschke, et al. [20] demonstrate experimentally that a sample with a rough surface can have low-angle intensities less than a third of those from the same sample after smoothing the surface with a flat plate. Surface roughness is a component of microabsorption: the higher the amount of microabsorption, the greater the significance of a rough surface. It is helpful here to clearly differentiate between absorption and microabsorption. Absorption describes the attenuation of x-rays as they pass through a homogeneous sample and is represented by the first term of the right side of Equation 21 ($I_0/2\mu$), while microabsorption P is an additional term that accounts for heterogeneity in the sample (i.e., large grain sizes and/or differences in μ between individual phases and the bulk).

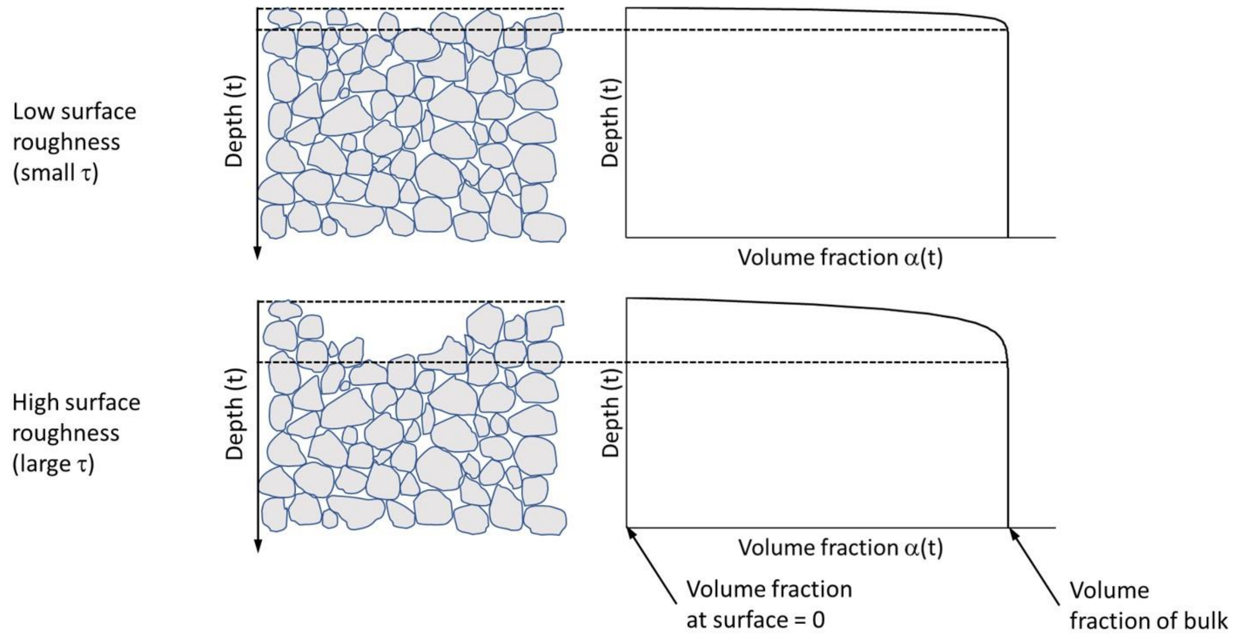

Figure 11. Surface roughness illustration, showing how the volume fraction of the sample changes with depth for a smooth vs. rough surface. The volume fraction vs. depth curves are described by the relation of Hermann and Ermrich [21], as stated in Pitschke, et al. [20] (Equation 26 below).

Building upon the works of both Harrison and Paskin [22] and Suortti [23], Hermann and Ermrich [21] present the reflected intensity (I') from a single phase sample with microabsorption P as

$$I' = I_0 \frac{1-P}{2\mu}, \qquad \text{Equation 21}$$

where P is written as the sum of an angle independent bulk term P_0 and an angle dependent surface term P_s. P_0 and P_s are expressed as

$$P_0 = 2\mu\beta(1-\alpha_0), \text{ and} \qquad \text{Equation 22}$$

and

$$P_s = 2\mu\beta\alpha_0\left(\frac{\tau}{\sin\theta}\right)\left(1-\frac{\tau}{\sin\theta}\right), \qquad \text{Equation 23}$$

where α_0 is the volume fraction of the bulk sample and β is related to the mean chord length $\bar{l}$ of the particles by

$$\bar{l} = \frac{-\beta}{\ln\alpha_0}. \qquad \text{Equation 24}$$

The surface roughness parameter τ is defined as

$$\tau = \frac{t_0}{\beta}, \qquad \text{Equation 25}$$

where t_0 is defined by the Hermann and Ermrich [21] expression for volume fraction α as a function of depth *t* into the sample:

$$\alpha(t) = \alpha_0 \left[1 - \mathrm{e}^{-t/t_0}\right], t > 0. \qquad \text{Equation 26}$$

As is shown in Figure 11, as t_0 increases, the change in volume fraction with depth becomes more gradual, corresponding to a rough surface. Pitschke, et al. [20] have rewritten the $1 - P$ of Equation 21 in terms of Equation 22 through Equation 26. It is presented as an angle dependent correction factor S_r:

$$S_r = 1 - P_0 - \frac{C\tau}{\sin\theta}\left(1 - \frac{\tau}{\sin\theta}\right), \qquad \text{Equation 27}$$

where S_r is the correction factor, and *C* is the collection of physical terms $2\mu\beta\alpha_0$. Pitschke, et al. [24] note that if the extent of microabsorption is small ($\mu\bar{l}$ <<1) and the surface is not too rough than P_0 and *C* are described exactly by their physical parameters.

TOPAS implements the correction factor shown in Equation 27 as a normalized form with only two refineable parameters. The normalization is achieved by dividing the correction factor by its maximum value (which occurs when $\sin\theta$ is equal to 1; i.e., θ is equal to 90°):

$$S_{Norm} = \frac{1 - P_0 - \frac{C\tau}{\sin\theta}\left(1 - \frac{\tau}{\sin\theta}\right)}{1 - P_0 - C\tau(1-\tau)}. \qquad \text{Equation 28}$$

From here both numerator and denominator can be divided by $1 - P_0$ and terms collected to give the following form:

$$S_{Norm} = \frac{1 - \frac{C\tau}{1-P_0}\left(\frac{1}{\sin\theta} - \frac{\tau}{\sin^2\theta}\right)}{1 - \frac{C\tau}{1-P_0}(1-\tau)}. \qquad \text{Equation 29}$$

Topas implements this form with the refineable parameters A_1 and A_2, where

$$A_1 = \frac{C\tau}{1-P_0}; \;\; A_2 = \tau. \qquad \text{Equation 30}$$

The final form of the correction factor in Topas is as follows:

$$S_{Norm} = \frac{1 - A_1\left(\frac{1}{\sin\theta} - \frac{A_2}{\sin^2\theta}\right)}{1 - A_1 + A_1 A_2}. \qquad \text{Equation 31}$$

It is useful to have an idea of what reasonable maximum values are for the refined parameters A_1 and A_2 in Topas, which lose physical significance as they become too large. Topas' default maximum and minimum for both A_1 and A_2 are 0.0001 and 1. These minimum values are reasonable, but the maximum values are not. Not only does allowing the surface roughness parameters access to the entire default solution space significantly increase computation time, but also fits with unreasonable parameters can be achieved. Figure 12 shows a proposed set of

conditions for a sample fit between 20° and 100° 2θ. Note that as the diffraction angle decreases, the expression decreases to a minimum value and then increases again. As a first limitation for a physical sample, it is not reasonable for this minimum to occur in or near the region where the sample is fit. The location of this minimum value is entirely dependent upon the A_2 parameter and can be identified by taking the derivative of the correction factor with respect to θ and setting it equal to 0:

$$\frac{d}{d\theta}S_{Norm} = \frac{d}{d\theta}\left(\frac{1-A_1\left(\frac{1}{\sin\theta}-\frac{A_2}{\sin^2\theta}\right)}{1-A_1+A_1A_2}\right),$$ Equation 32

$$0 = \frac{d}{d\theta}\left(\frac{1}{\sin\theta} - \frac{A_2}{\sin^2\theta}\right),$$ Equation 33

$$0 = -\csc\theta\cot\theta - A_2(-2\csc^2\theta\cot\theta).$$ Equation 34

Some manipulation leads to the expression

$$A_2 = \frac{\sin\theta}{2}.$$ Equation 35

With this expression, the value of A_2 that will give the minimum at a desired angle θ is easily obtained. For a fit starting at 20° 2θ, it seems reasonable to place the minimum at 10° 2θ, or $\theta = 5°$. The corresponding A_2 value is 0.044. A potentially more accurate limitation of the value of A_2 could be obtained by identifying the inflection points of the correction factor by taking the second derivative of the expression and setting it equal to 0. The resulting expression could be used to ensure that the inflection point on the high-angle side of the minimum stays outside the fit region.

A limitation can be placed on the maximum value of A_1 by assuming that the correction factor cannot be negative. The value for which this occurs can be found by setting the correction factor equal to zero and solving for A_1 (using the value of A_2 found above). The result for this example gives $A_1 = 0.17$. Even with boundary conditions such as these maximum values for A_1 and A_2, we recommend always graphing S_{Norm} vs 2θ over the fit region to verify that the refined A_1 and A_2 parameters make sense.

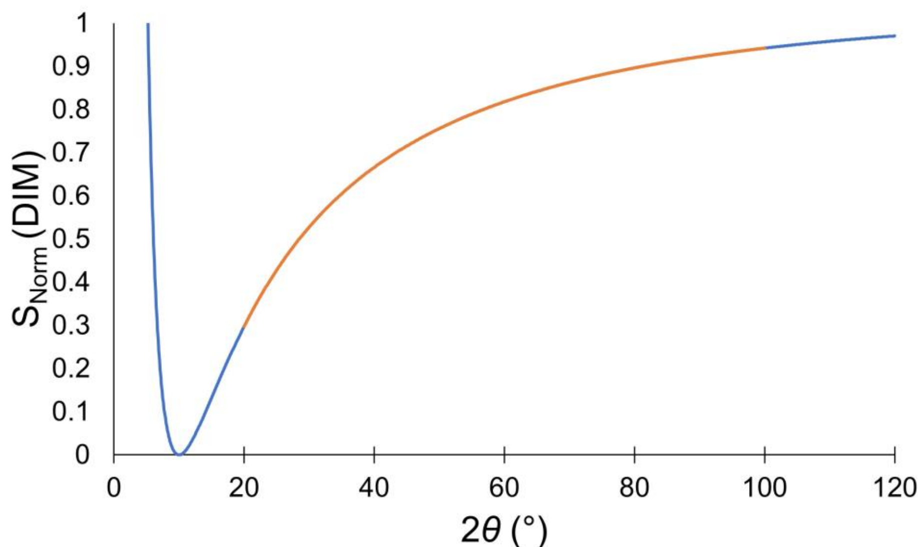

Figure 12. [20,] Pitschke, et al. [24] correction (Equation 31) as implemented in TOPAS with A_1 = .1743 and A_2 = .043578

Modifying the standard XRD experiment

In light of the intensity effects discussed above and the requirements for their correction, we now compile the modifications needed for a benchtop XRD experiment designed to characterize ultra-small, supported nano-crystals.

1. All diffractograms need to be normalized to an external standard. This can be achieved by running the standard immediately before and after each diffractogram is measured.
2. Diffractograms will need to be measured for the empty sample holder, pure support, and a highly crystalline material with high $\bar{\mu}$. An additional diffractogram of a highly crystalline material with $\bar{\mu}$ equivalent to the nano-crystal sample may also be needed.
3. The mass of all samples must be recorded. Because some mass can be lost during sample preparation, recording the mass after the measurement is recommended. Ideally, the mass of the support phase should be equal between samples; measuring target masses into the sample holders can help achieve this.
4. All samples should be measured in the same sample holder.
5. The dimensions of the sample holder should be carefully measured and recorded.
6. Care should be taken to make sure that the surface of nanoparticle samples is flat and smooth. Samples should be ground prior to loading the sample holder. See the videos in the supplementary information for detailed instructions on preparing samples for the XRD.

Errors in analysis

Once the diffractograms have been collected for the nanoparticle sample and pure support, the nanoparticle counts have been isolated from the support, the reader's analysis software has been updated to correct for the afore-mentioned intensity effects, and data (with error information, see the "Statistical Errors" section in the SI) has been imported along with structure files of interest,

the reader is ready to begin analysis. While we leave the particulars of the analysis up to discretion the reader, we do offer some pointers about errors and how readers may choose between different fits.

Errors may be separated into two categories: statistical errors (errors due to uncertainty in the counts; these errors decrease with increased counts – i.e. stronger signal or longer dwell times) and systematic errors (examples of these errors include "bias introduced by some undescribed physics in the experiment or an inadequate background, peak-shape or structural model" – McCusker, et al. [25]).

Statistical errors can be estimated and included in a Rietveld refinement; these errors influence the R_{wp} and R_{exp} "quality of fit" parameters. In Topas, statistical errors can be imported together with the 2θ and intensity information as an xye file (users of the commercial version of Topas V6 will need to install a software update available on Brukersupport.com in order to import the error information from an xye file (Lipp and Coelho [26]). If error information is not imported, Topas' default is to take the square root of the intensity. This is fine if the diffractogram being analyzed has intensity in total counts and has not been modified in any way (e.g. normalized or background subtracted), but if not the errors should be calculated and imported (otherwise the R_{wp} and R_{exp} parameters will not be accurate). One advantage of importing the errors is that the nanoparticle scattering can be isolated prior to analysis, thus allowing the user to directly view how calculated fits match to the isolated nanoparticle diffractogram (i.e. background and support subtracted).

Systematic errors cannot be estimated. It is the purpose of this work to help readers reduce systematic errors arising from background subtraction and intensity effects. Other sources of systematic errors (e.g. incorrect phase identification, size distributions, changes in oxide lattice parameter, thermal displacement parameters, etc.) may still be present and will depend on the analysis method (e.g. details of the Rietveld refinement).

In choosing between fits, we defer to the statements of McCusker, et al. [25]: "The most important criteria for judging the quality of a Rietveld refinement are (i) the fit of the calculated pattern to the observed data and (ii) the chemical sense of the structural model." Quality of fit parameters such as R_{wp} can be useful in comparing fits for a single sample, but should not be substituted for visually inspecting the fits against the isolated nanoparticle diffractogram. The fits should also make sense – readers should compare their results with other literature and (if possible) corroborate results with complementary analysis techniques.

Case Study: 4.8% Pt / amorphous silica

A 4.8 wt% Pt / amorphous silica sample prepared with the strong electrostatic adsorption method (Schreier and Regalbuto [27], Miller, et al. [28]) and aged under ambient conditions is presented as a case study demonstrating the capabilities of benchtop x-ray diffraction when the methods presented in this work are applied. Full details of the experimental methods are provided in the supplemental information. The results are corroborated with STEM and XAS.

STEM

Figure 13 shows a representative STEM image and accompanying size distribution of the 4.8% Pt / A300 sample. Over 1700 particles were measured by hand to produce the size histogram displayed in the inset. The results show a narrow size distribution with no observed particles larger than 2.7 nm. The resulting number-weighted average (D_N), surface-weighted average (D_S), and volume weighted average (D_V) are 1.1 nm, 1.2 nm, and 1.3 nm respectively. The volume weighted average corresponds to the XRD particle size (which is a volume-weighted technique). It is noted that because not all of the Pt nanoparticles are fully in focus in the images, these presented particle sizes (based on the projected area in the images) are an upper estimate of the particle size. The actual sizes of the measured particles in the electron beam are likely somewhat smaller (Xia, et al. [29]).

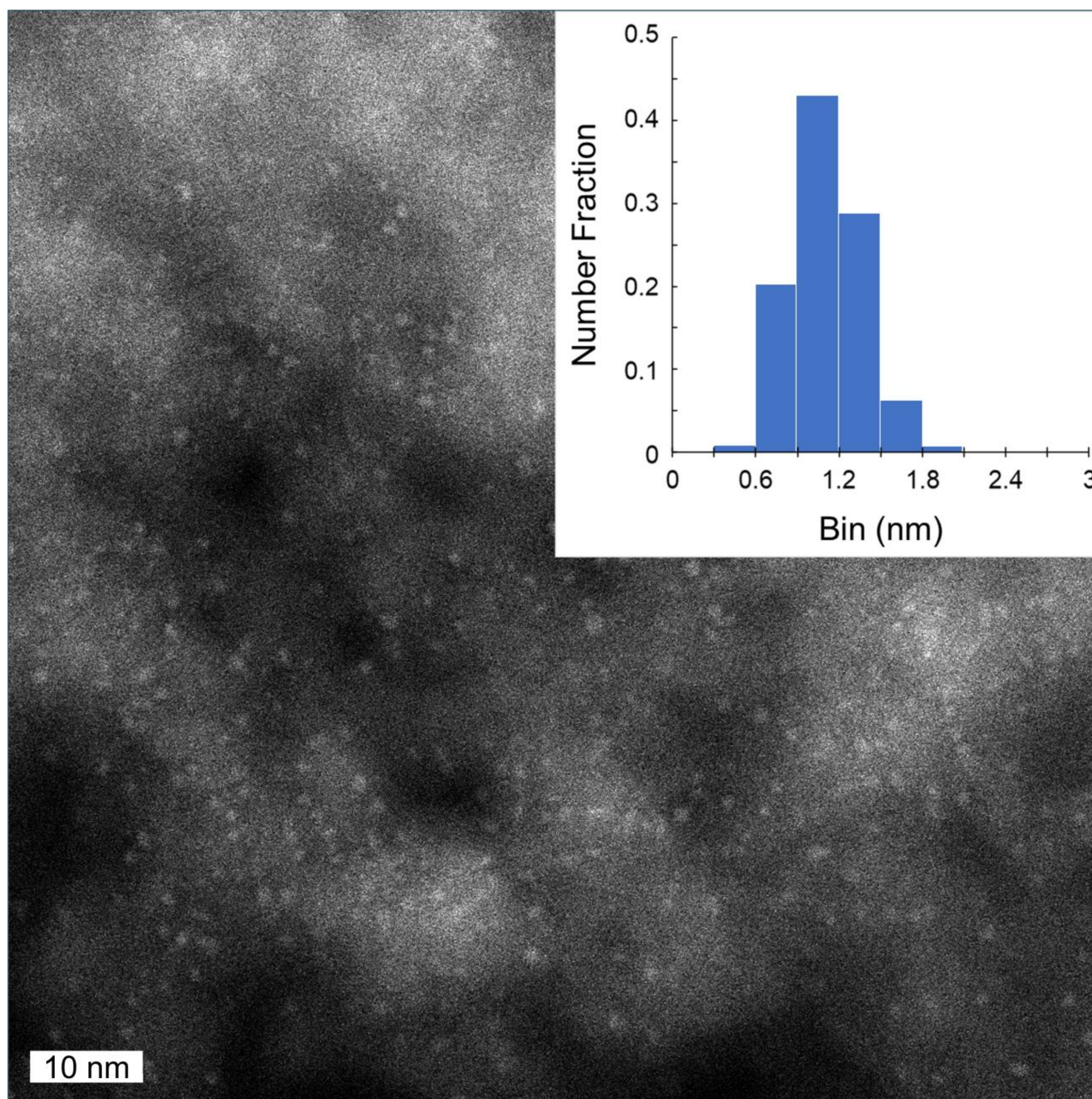

Figure 13. A representative STEM image of the 4.8% Pt / A300 sample. Over 1700 particles were measured to produce the included size distribution.

XRD

A detailed discussion of the experimental methods used for XRD is provided in the supplemental information. A brief description now follows. Figure 14 depicts the major steps in isolating the nanoparticle scattering from the support scattering. First, the 4.8% Pt / silica sample, pure silica (treated with the same SEA, drying, and reduction treatment as the Pt sample), and empty sample holder were each scanned six times against the NIST 1976c intensity standard. The results were corrected for intensity drift and averaged together. The errors for the 4.8% Pt / silica sample were calculated and saved together with the 2θ and intensity information in an xye file as described in the supplemental information. A spline was fit to the empty sample holder

contribution using Fityk (Wojdyr [30]), (A). Once the spline was subtracted from the Pt / silica sample and pure treated support (B) the support diffractogram was adjusted to match the absorption and finite thickness calculated for the Pt / silica sample (C). In this step, it was determined that a total volume ratio of 1.06:1 (pure support sample:nanoparticle sample) would result in reasonable Rietveld fits. Finally, the estimated spline was added back to the adjusted diffractograms (D). Note that the Pt / silica diffractogram is unchanged by this process; only the support diffractogram is adjusted.

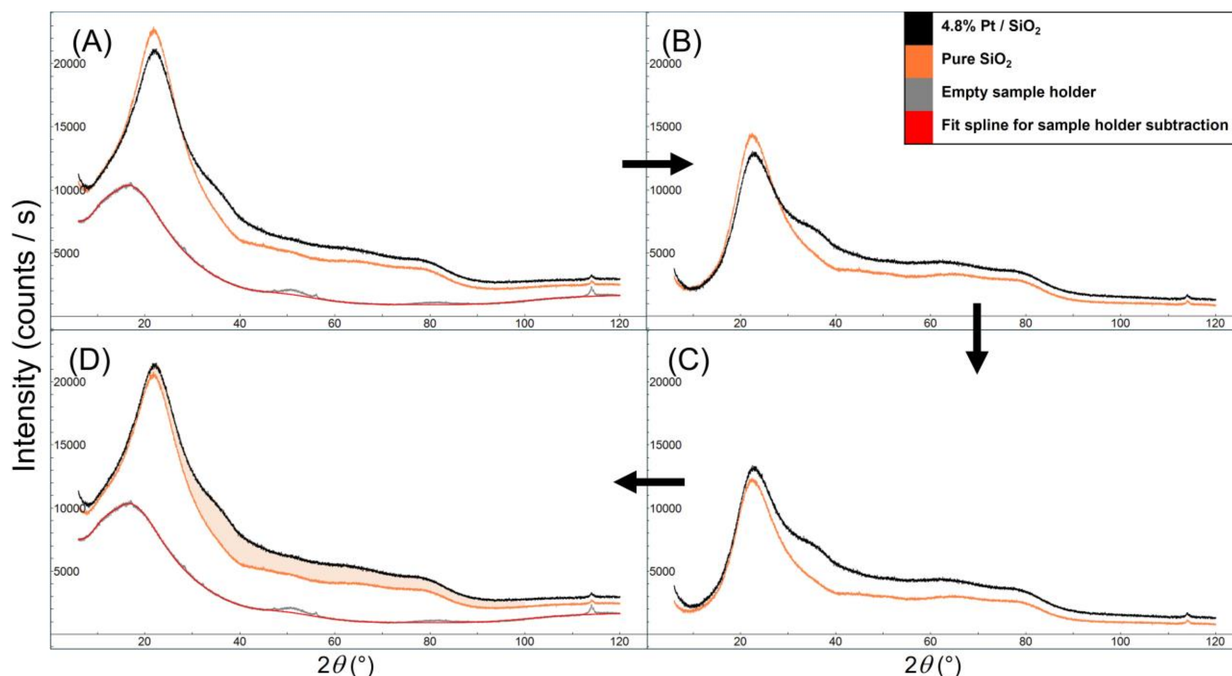

Figure 14. Background subtraction procedure for 4.8% Pt / SiO_2. (A) Data after adjusting for drift and averaging multiple runs. (B) Data after subtracting the estimated sample holder contribution (fit spline, shown in red). (C) Data after correcting for differences in absorption and finite thickness. (D) Data after adding back the estimated sample holder contribution (for analysis in Topas). The region of the total calculated fit is shaded; see Figure 15 for the support subtracted Rietveld fit.

For the analysis in Topas, the software was first updated so that error information could be imported via xye files (see below). The macros for Lorentz-polarization, absorption, surface roughness, and beam spill were then adjusted to scale peaks on a point-by-point basis (the Lorentz-polarization macro also had an error that was corrected; see the supplementary info for more information and for a complete list of modifications made to the Topas macros). The beam spill macro was also updated to include the 2D correction for circular sample holders. The updates to the code were made directly in the topas.inc file; this was found to be the most functional method of implementation (we note, however, that users may prefer to use methods that do not modify the topas.inc file, e.g. by using a “local.inc” file). For the Rietveld analysis, the adjusted support diffractogram was first subtracted from the Pt / silica diffractogram; this was done by fitting the adjusted support with a high-order Chebyshev polynomial in Topas and then subtracting the Chebyshev polynomial from the Pt / silica diffractogram using Microsoft Excel. The Pt nanoparticle scattering was isolated to allow better visual examination of fits during refinement; using a Chebyshev polynomial to describe the support with minimal noise allowed us to assume the background subtraction had negligible effect on statistical errors. The support subtracted Pt /

silica diffractogram was then imported as an xye file (users of the commercial version of Topas V6 may need to download and install a fix from Brukersupport.com to allow proper loading of the error information from an xye file – see the supplementary information and Lipp and Coelho [26] for more details). Twelve Pt and Pt oxide structure files (Table 2) were fit individually and in combinations using fundamental parameter peaks with only the overall scale factor and a Gaussian size broadening convolution allowed to refine for each phase (an additional Lorentzian size broadening convolution was found to have very little effect on the results so it was removed from the analysis for simplicity, see "Notes on peak broadening" in the Supplementary Information for more information). Temperature factors were fixed at their imported / default values (in most cases $Beq. = 0$). Once the most promising combinations of phases were identified, additional parameters (i.e. the Pt metal lattice parameter and two surface roughness terms) were allowed to refine.

Table 2. Pt / Pt oxide phases investigated with XRD

Phase	Space Group	H-M*	ICSD #	Referemce
Pt	225	$Fm\bar{3}m$	52250	Owen and Yates [31]
PtO	131	$P42/mmc$	26599	Moore Jr and Pauling [32]
PtO	225	$Fm\bar{3}m$	105543	Kumar and Saxena [33]
PtO_2	58	$Pnnm$	202407	Range, et al. [34]
PtO_2	136	$P42/mnm$	647316	Fernandez and Chamberland [35]
PtO_2	164	$P\bar{3}m1$	24922	Hoekstra, et al. [36]
PtO_2	186	$P63mc$	24923	Hoekstra, et al. [36]
PtO_2	205	$Pa\bar{3}$	251568	Shirako, et al. [37]
PtO_2	224	$Pn\bar{3}mS$	77654	Kumar and Saxena [33]
Pt_3O_4	223	$Pm\bar{3}n$	30444	Muller and Roy [38]
Pt_3O_4	229	$Im\bar{3}m$	27836	Galloni and Roffo Jr [39]
$Pt_{3.4}O_4$	223	$Pm\bar{3}n$	200053	Grande and Müller-Buschbaum [40]

* Hermann-Mauguin notation

Fits were compared by visual inspection, chemical/physical sense, and simplicity. R_{wp} values were helpful to compare fits containing the same number of refined parameters (i.e. the R_{wp} values of two-phase fits should not be directly compared with those of three-phase fits). The best fit in terms of the above criteria achieved with a combination of two phases is shown in Figure 15. The result suggests that the nano-crystallites consist of a combination of Pt and PtO_2, both with sub-nanometer crystallite sizes. The error bars shown come from comparing different fits, and are more than three times greater than the Topas-generated error values (which are based on singular value decomposition).

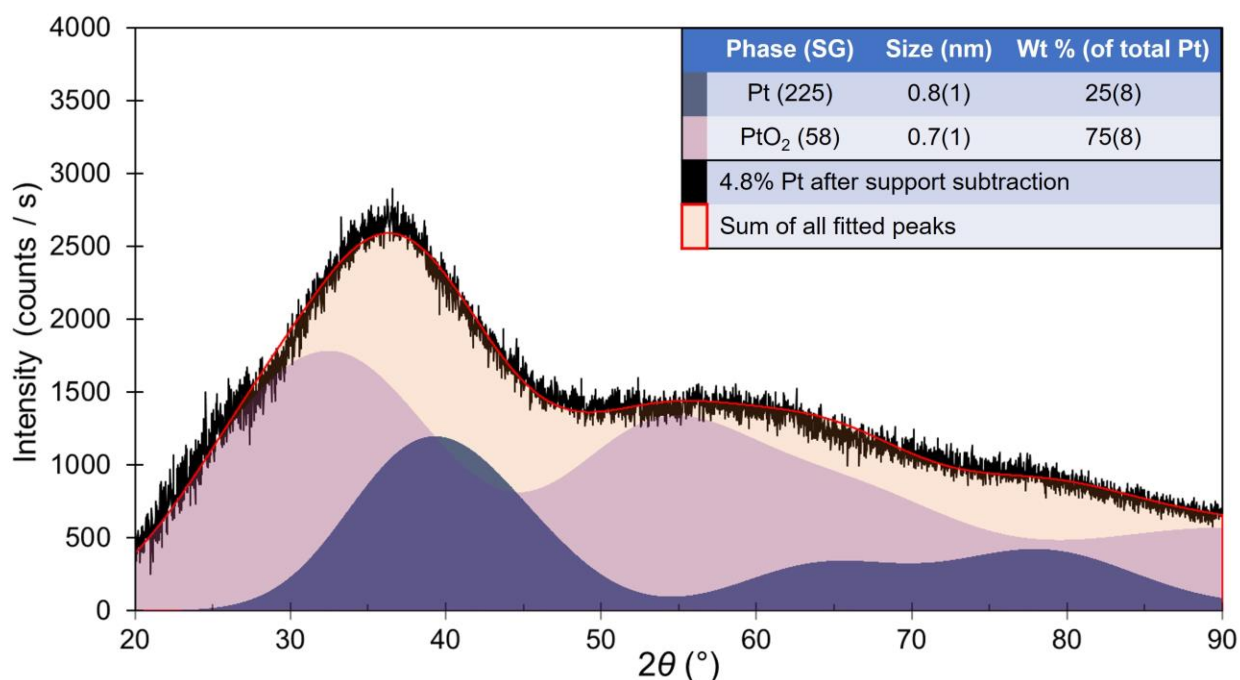

Figure 15. Aged 4.8% Pt sample in air, after background subtraction. In the shown fit, only seven terms were allowed to refine: the Gaussian size broadening and overall scale factor for each phase, the Pt metal lattice parameter (L.P. = 4.05(3) Å), and two terms adjusting the intensity for surface roughness. All other terms were fixed, as described in the experimental methods in the supplementary information. The shown fit has Rwp = 5.69 (Rexp = 4.96).

Surface oxide phase

There have been previous reports of small Pt nanoparticles oxidizing in air at room temperature, though the reports do not agree on the identity of the oxide. Bucher, et al. [41] used ^{195}Pt NMR on a 5.7% Pt / SiO_2 sample (consisting of slightly larger particles than our sample: D_S = 1.7 nm) to identify the oxide as PtO_2 (phase not specified). Gnutzmann and Vogel [10] used a Guinier XRD on a 6.3% Pt / SiO_2 sample (D_N = 1.3 nm, D_V = 1.6 nm) and identified the oxide as primarily PtO with <10% Pt_3O_4. Banerjee, et al. [42] used STEM, XPS, and a benchtop XRD with LPSD detector to investigate many Pt samples supported on carbon and silica supports. They tentatively attributed the oxide phase to Pt_3O_4, even though the phase's second strongest line at 22.5° 2θ was missing from the diffractograms. We also note that their STEM and XPS experiments took place in ultra-high vacuum – this is known to be a reducing environment and may have partially reduced the samples as compared to ambient conditions.

In this work, the background-subtracted 4.8% Pt / SiO_2 XRD (Figure 15) is fit well with two phases: a metallic Pt phase (space group 225, $Fm\overline{3}m$) and ß-PtO_2 (orthorhombic, space group 58, *Pnnm*). This is in agreement with the extended x-ray absorption fine structure (EXAFS); it is noted that the EXAFS analysis also identified α-PtO_2 (trigonal, space group 164, $P\overline{3}m1$) as a possible fit. However, α-PtO_2 did not provide as good a fit for the XRD (Figure 16), giving unreasonable results for the metallic Pt particle size (0.3 nm) and wt% (~60%). While the identification of PtO_2 agrees with the results from Bucher, et al. [41], it does not seem to agree with the findings of Gnutzmann and Vogel [10] and Banerjee, et al. [42]. We now point out that the quality of the background subtraction can have a significant effect on phase identification. Gnutzmann and Vogel [10] adjust for differences in absorption between their sample and support, but close

inspection of their results (Figure 4 in [10]) reveals that the absorption correction was only applied to match the silica peaks at ~20° 2θ, rather than account for the full difference in absorption. Their resulting background subtraction falsely indicates that there is no diffraction signal on top of the silica peak, leading the authors to choose PtO as the best fit to their patterns. Banerjee, et al. [42] did not account for absorption and other angle-dependent intensity factors, using instead a simple normalization to similarly match the silica peaks. The resulting background subtractions leave artifacts in the diffraction pattern; thus making it necessary to decompose the pattern on a peak-by-peak basis.

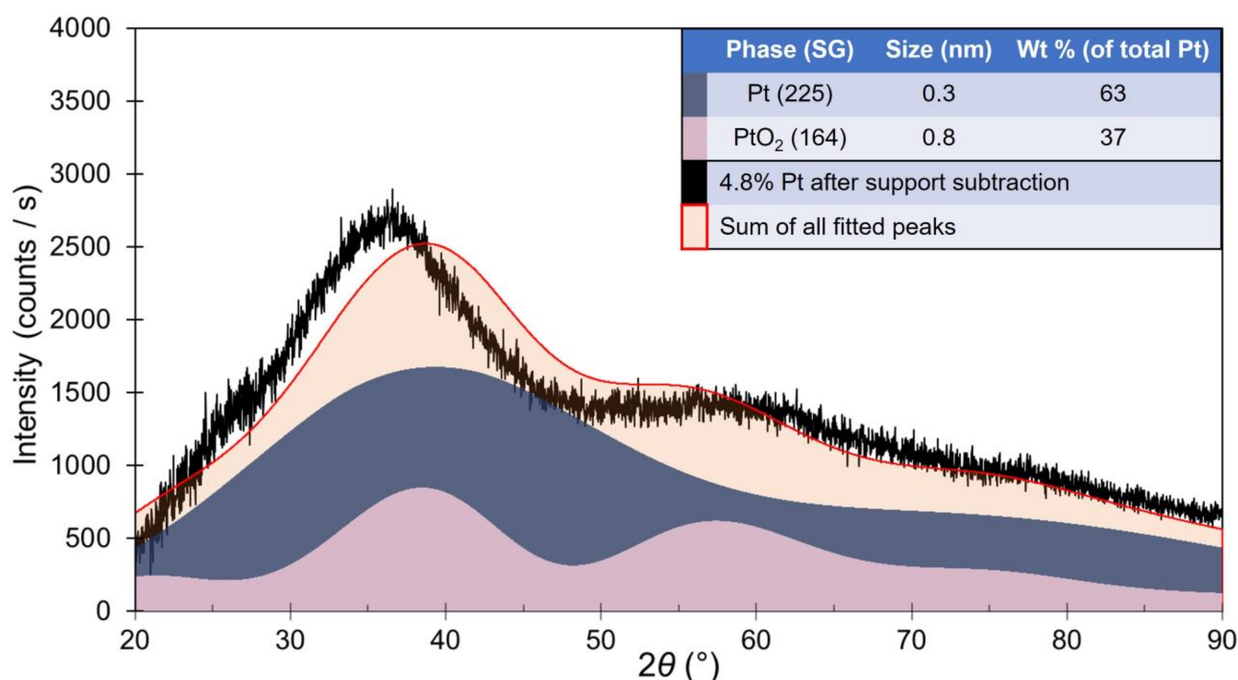

Figure 16. 4.8% Pt / SiO_2 fit with α-PtO_2. The shown fit includes corrections for Lorentz-polarization, beam spill, absorption, and finite thickness. There are seven refined parameters: scale and Gaussian size for each phase, Pt lattice parameter (L.P. = 3.80 Å), and two terms for surface roughness. The shown fit has Rwp = 14.37 (Rexp = 4.96).

Lattice Parameter

A second factor affecting the oxide phase identification is whether the Pt lattice parameter is allowed to refine. Gnutzmann and Vogel [10], Banerjee, et al. [42], and this work all observe that the main Pt / SiO_2 nanoparticle sample diffraction peak is apparently centered between 36° and 38.5° 2θ, more than a full degree below the main (and lowest angle) peak of bulk Pt (39.8° 2θ). Neither Gnutzmann and Vogel [10] nor Banerjee, et al. [42] allowed the Pt lattice parameter to refine to fit this peak. Rather, Banerjee, et al. [42] attribute it to a Pt peak superposed with a Pt_3O_4 (210) peak (space group 223, $Pm\bar{3}n$) centered at 35.9°, while Gnutzmann and Vogel [10] fit the whole pattern to a majority of Pt and PtO, with minor amounts of Pt_3O_4. We similarly can achieve a good fit using small amounts of Pt_3O_4 (Figure 17) with Pt and ß-PtO_2. However, the size of the apparent Pt_3O_4 crystallites (1.5nm) does not make sense in relation to their <10% contribution to the background subtracted Pt diffractogram. Perhaps the most unexpected result of this work is that an excellent fit of the entire pattern (Figure 15) can be achieved with only Pt and ß-PtO_2 by allowing the Pt lattice parameter to refine to larger values (corresponding to longer Pt-Pt bond distance, i.e. a

dilated Pt lattice). The resulting LP is 4.045 Å [d (111) = 2.335 Å, 38.52° 2θ], a 3.1% increase over the bulk value (3.9237 Å). In this case the peak centered around 36° is composed primarily of the Pt (111) peak and the ß-PtO_2 (011) peak (d = 2.580 Å, 34.74° 2θ). We postulate that the documentation of Pt_3O_4 by Banerjee, et al. [42] using fast Fourier transform (FFT) of atomically resolved STEM images may similarly result from an expanded metallic Pt lattice combined with the presence of PtO_2 – though the reducing environment of the UHV and electron beam may also play a role.

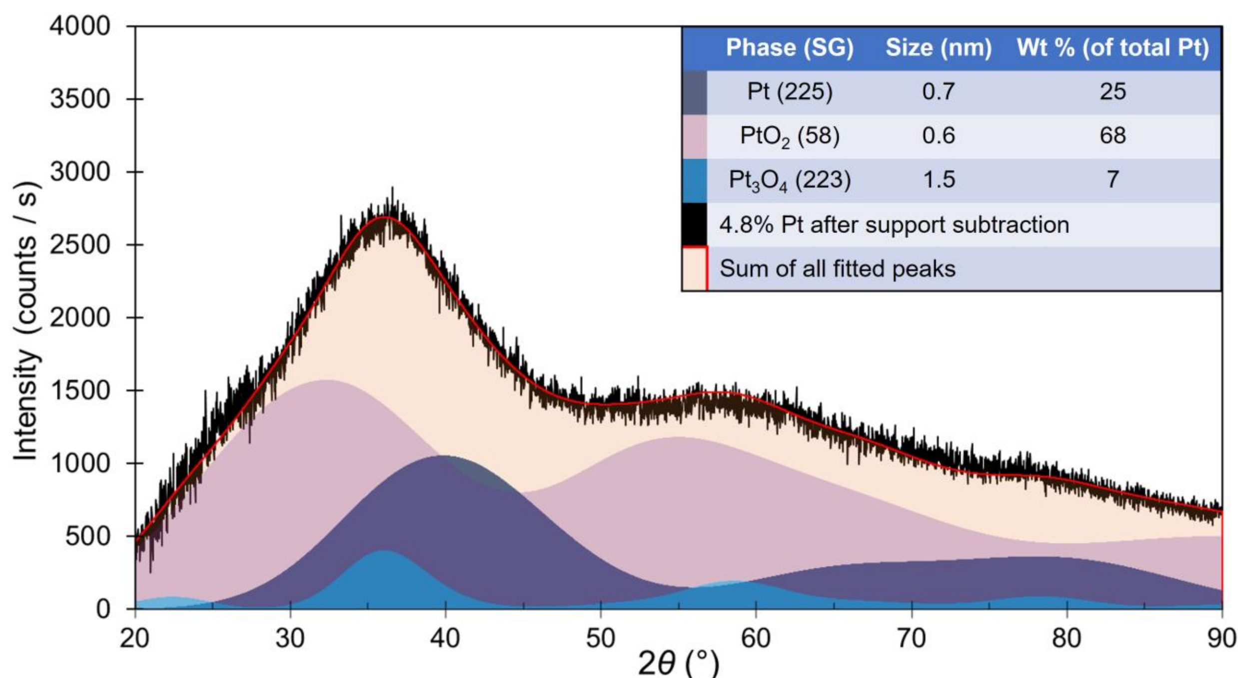

Figure 17. 4.8% Pt / SiO_2 deconvolution with Pt_3O_4. The shown fit includes corrections for Lorentz-polarization, beam spill, absorption, and finite thickness. There are nine refined parameters: scale and Gaussian size for each phase, Pt lattice parameter (L.P. = 3.98 Å), and two terms for surface roughness. The shown fit has Rwp = 5.77 (Rexp = 4.96).

This lattice expansion (i.e. dilation) at first seems to contradict the general observation in literature that as nanoparticles decrease in size their lattice parameters contract (e.g. Miller, et al. [2], Lamber, et al. [43]). A closer look at the literature shows that there are several counter-examples documenting dilation instead. For example, Goyhenex, et al. [44] examined Pd nanoparticles epitaxially grown on an MgO (100) surface with surface electron energy-loss fine-structure spectroscopy under UHV conditions and observed up to 6% lattice dilation with decreasing particle size; the effect was attributed to pseudomorphism that the authors defined as a "perfect accommodation between the particles and substrate lattices"; i.e. at the interface between the nanoparticles and support the Pd nanoparticle lattice expanded to perfectly fit into the MgO (100) lattice. Jacobs and Schryvers [45] examined Pd nanoparticles photodeposited onto a thin film of anatase TiO_2 with high resolution electron microscopy and observed lattice dilation up to 10% greater than bulk in the smaller nanoparticles; after heating in oxygen the maximum lattice dilation observed was up to 15% greater than the bulk. The authors attributed the lattice expansion to oxygen dissolved into the Pd lattice. Du, et al. [46] examined 2.5 to 5.0 nm Pt nanoparticles, both supported on carbon and unsupported with high-resolution transmission electron microscopy. The authors documented Pt-Pt bond distance as a function of position inside a nanoparticle, and found

that a surface oxide layer caused extensive lattice expansion near the surface of the nanoparticle which in turn caused the core lattice to expand beyond bulk values. Finally, Gallagher, et al. [3] examined Pt nanoparticles supported on alumina in-situ using synchrotron techniques including x-ray absorption spectroscopy (XAS), pair distribution function (PDF), and x-ray diffraction (XRD). They observed lattice contraction as a function of decreasing particle size for the fully reduced particles, but observed lattice expansion when the largest nanoparticles were measured in air with XRD (they were unable to examine the smaller nanoparticles in air with XRD due to difficulty in subtracting the background and in separating oxide phases from the metallic Pt). We summarize the literature in the following statement: as nanoparticle sizes become small their lattice parameters become more susceptible to influences that drive them away from bulk values. The smaller the nanoparticle, the less its lattice parameter/s can be assumed to match the values documented for its bulk counterpart. Whether the lattice parameter contracts or dilates or even whether the nanoparticle changes phase depends on the outside influences on the particle. Because nanoparticle lattice parameters are so susceptible to change depending on the environment, it is important to be able to characterize these systems in-situ. It is challenging for instruments that require ultra-high vacuums such as electron microscopy and XPS to examine samples under ambient conditions; for systems where oxidation is suspected this is especially problematic since ultra-high vacuum is known to be a reducing environment. XRD does not share this limitation and can be used to directly characterize samples under a multitude of environments – the simplest of which are ambient conditions.

We now note an apparent contradiction between our XRD and EXAFS results: our EXAFS analysis indicates a lattice parameter contraction (3.66 Å, -6.7%, see below) compared to the bulk (3.92 Å), rather than the expansion observed with XRD (4.05 Å, +3.3%). One possible explanation is that for XRD the "as received" sample was measured in air, while the EXAFS sample was measured after stabilizing in a flow of He, during which there is a slight change in the white line intensity. Interestingly, comparisons with the results of Gallagher, et al. [3] indicate a similar discrepancy between EXAFS and XRD for oxidized Pt: lattice expansion with XRD and lattice contraction with EXAFS – but in their case both methods measured the oxidized sample in air.

Size and extent of surface oxidation

The XRD fit with Pt and ß-PtO_2 (Figure 15) suggests roughly 20% Pt crystallites around 0.8 nm in size and 80% ß-PtO_2 crystallites around 0.7 nm in size. It is noted that the estimated size of each phase depends on the structure and parameters included in the fit; variations of as much as 0.1nm were observed. It is interesting that the sum of these two dimensions approximates the STEM volume-weighted size of 1.3 nm (as also noted by Banerjee, et al. [42]) and the EXAFS-determined value of the fully reduced sample with an average particle size of ~1.3nm. In the following discussion we compare the combined Pt / Pt oxide structures in terms of the number of Pt atoms. We can estimate an upper limit for the number of atoms present in the average nanoparticle by assuming that in the STEM environment the nanoparticles are fully reduced (PtO_2 has approximately half the amount of Pt atoms per unit volume). With this assumption, and making use of the Pt and ß-PtO_2 unit cell volumes and number of Pt atoms per unit cell (Pt: unit cell = 60.407 $Å^3$, 4 Pt atoms per cell; ß-PtO_2: unit cell = 63.818 $Å^3$, 2 Pt atoms per cell) the STEM result of 1.3 nm particles gives 76 atoms for a spherical particle (38 atoms for a hemisphere). If we

assume a Pt core - Pt oxide shell model with the XRD dimension of 0.84 nm as the diameter of the core (0.84 nm, 21 atoms for a sphere), then 76 total Pt atoms is consistent with an oxide shell containing 55 atoms and around 0.4 nm thick. This is smaller than the XRD ß-PtO_2 size of 0.7 nm (0.66 nm); however, it is noted that the thickness of a shell presents the shortest possible distance that X-rays can interact with the shell's atoms; the longest possible distance is along the chord tangent to the core (Figure 18). In this model the maximum distance would be 1.4 nm. The average distance x-rays interact with the shell would therefore be somewhere in-between; this is consistent with our result. The mass fraction of each phase can also be calculated from the core-shell model: a 21 Pt atom core and 55 Pt atom shell (with 110 corresponding oxygen atoms) results in 24 wt% Pt and 76 wt% PtO_2. This is consistent with the XRD and x-ray absorption near edge structure (XANES) results.

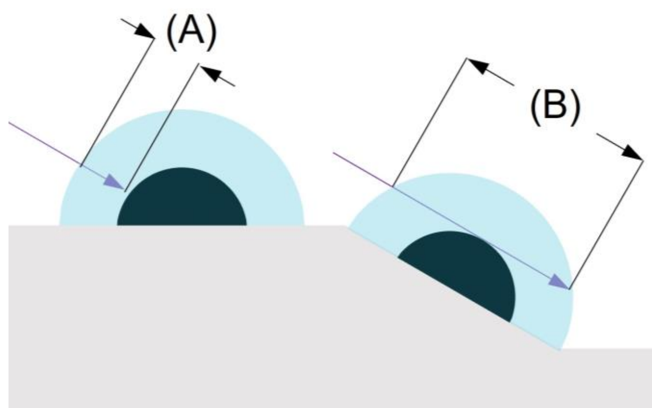

Figure 18. The distance an x-ray travels through a material in a shell depends on where it strikes. (A): minimum distance traveled. (B): maximum distance traveled.

XAS

An in-situ XAS (EXAFS, and XANES) experiment was conducted on the 4.8% Pt / SiO_2 sample to corroborate the XRD findings. The sample was first measured "as-prepared", followed by desorption and reduction. Details on the experimental methods and results can be found in the supplemental information. The main findings are summarized below:

- Linear combination fitting using bulk standards suggests the as-prepared state consists of ~34% Pt metal and ~66% PtO_2
- The as-prepared state (prior to reducing the sample) was consistent with a metallic core surrounded by an oxide shell
- In the as prepared state the EXAFS results show a Pt-Pt contraction in the Pt metallic core (2.59Å) compared to Pt foil (2.77Å)
- In the reduced state, the Pt is fully reduced. EXAFS results show the Pt – Pt bond length is 2.73Å
- The Pt cluster size in the reduced state is estimated using the method of Jentys [47] to be ~1.3nm containing 76 atoms, which is in remarkable agreement with the STEM results

- Results for the oxidized catalyst indicate a cluster of less than 10 atoms with an estimated size less than 1nm for the metallic core; EXAFS is not able to estimate the size of the oxide shell

Discussion

Applications of the method

- *Studies of simple nano systems*. In practice, characterizing ultra-small crystallites with x-ray diffraction is challenging – a fact that is echoed by the current state of the field. Gallagher, et al. [3] sought to determine the conditions under which 2.8 wt% Pt / Al_2O_3 nanoparticles (1-2nm) could be characterized with Bragg diffraction. They concluded that such particles could only be analyzed when reduced – the nanoparticles could not be detected under ambient conditions due to the oxidation of the nanoparticles. They also concluded that the increased signal to noise ratio provided by synchrotron radiation was required to investigate such systems (< 3nm), a point that was emphatically reiterated in later papers examining different bimetallic Pt-containing nanoparticles (2 to 3 nm) supported on silica (Wu, et al. [48], Ma, et al. [49], Wu, et al. [50]). This work demonstrates that - for simple nano systems - neither synchrotron radiation nor full reduction of the nanoparticles is required. We show that even sub-nanometer crystallites may be characterized with Bragg diffraction by benchtop equipment. We further demonstrate that characterization is possible when metal and oxide phases are present in the same sample. However, more challenging nanoscale systems, e.g., those with multiple elements / phases, may not be possible to decompose.
- *Independent estimation of weight loading*. For a single metal, the effect of x-ray absorption on the support may be used to give an independent estimate of the weight loading. If the methods presented in this work are applied, a sample of unknown weight loading might be estimated by determining the value of μ needed for the unknown sample so that the pure support (with known μ) can be corrected to match it. Once μ is known for the unknown sample, the corresponding weight loading can be determined. The feasibility of this would depend on the difference in μ between the support and elements of unknown weight loading (the larger the difference, the more accurate the estimate). The feasibility would also depend on how well the diffractogram of the unknown material could be separated from the support.
- *Crystalline supports*. The methods presented in this work also apply to crystalline supports. However, it must be noted that any change in the vertical displacement of the sample (i.e. height error or displacement error) will cause an angle-dependent shift of the Bragg peaks that must be corrected. Further details can be found in Dinnebier, et al. [18], page 24, and in Lipp [51]. Future work is planned to further demonstrate XRD analyses with crystalline supports.

Limitations of the method

- *Limitations of Rietveld Refinement.* While the results obtained using the simple core-shell model are useful, the amount of information that can be obtained from the data using Rietveld refinement is limited. There are two types of coherent elastic scattering that occur in an XRD experiment: Bragg diffraction and diffuse scattering (Dinnebier, et al. [18]). Rietveld refinement operates solely with Bragg diffraction. Diffuse scattering becomes more important as crystallite sizes decrease; Debye Function Analysis (DFA) includes both Bragg and diffuse scattering and is especially powerful in the atomic to nanometer size range and for characterizing a broad range of defects (Bertolotti, et al. [52]). One particular strength of DFA is the determination of probability distributions (e.g. size distributions). DFA can be performed on XRD data obtained with Bragg-Brentano geometry; one challenge is the proper subtraction of the background (Pakharukova, et al. [53]). The intensity correction methods presented in this work could similarly be applied before DFA analyses and therefore aid in their background subtractions. It is noted that the greater simplicity of Rietveld analysis gives it an advantage over DFA in terms of providing characterizations with quicker turn-around times (especially useful for commercial applications). Rietveld refinement may also serve as a companion to DFA: the simpler analysis quickly narrowing the scope of a system prior to the more detailed and complex method.
- *The "pure" support must be available as a separately measurable entity*. To accurately subtract the background, any non-nanocrystal part of the sample (designated with the term "support" in the following discussion) must be measurable in a separate XRD experiment. The presented method for background correction and subtraction assumes that the support is a separate entity from the nano crystallites, i.e., the nano crystallites do not physically change the support in any significant way. If this is not true and / or a sample of the "pure" support (without nano crystals) is not available, then the background subtraction method may not be accurate. For the 4.8% Pt / SiO_2 case study presented in this work, it is reasonable to assume that the effect of the nanoparticles on the support is negligible. If each Pt atom directly affects a silicon atom, then only 0.7 wt% of the silica support will be affected.
- *The elemental composition of the sample must be known (weight loadings)*. Another limitation of the background subtraction method is that the quantitative elemental composition of the sample must be known to calculate the x-ray absorption and finite thickness effects. For unknown samples, the bulk elemental composition must first be measured, e.g., with an x-ray fluorescence (XRF) analysis or ICP-OES. Surface sensitive techniques such as x-ray photoelectron spectroscopy may not give an accurate representation of the elemental composition if the surface composition is different from the bulk.
- *Only pre-defined structures can be compared*. One of the strengths of Rietveld refinement for bulk materials is the possibility to determine the crystal structures of unknown phases. This is not applicable at the nanoscale since the peaks merge and other nano-effects become prominent. Only existing or hypothetical crystal phases can be fit to

the data; the best fits are assumed to be the closest to the true structure. If the nano-crystallite consists of an unknown phase for which the analyst has no matching structure, then characterization may not be possible.

- *The angle dependence of the atomic form factor is not corrected point-by-point*. There is an additional angle-dependent intensity factor that is not corrected for in this work: the atomic form factor. This intensity factor is highest at low angles and decreases with increasing θ, causing peak-pulling towards lower angles for broad peaks (Kaszkur [54]). For a Pt (111) peak with size broadening corresponding to a 0.87 nm domain size (the same conditions used to estimate the peak-pulling effects displayed in Table 1), the estimated peak pull is -0.1 ° - placing it among the least significant peak-pulling effects (a full order of magnitude lower than the Lorentz-Polarization effect). Topas does not allow for the form factor to be simply calculated on a point-by-point basis (as is the case for the other angle-dependent intensity effects); by default, in Topas the form-factor is calculated based on a peak's nominal center (d-spacing). The error introduced by not accounting for the peak-pull of this intensity effect is expected to be small; still, future work could be done to allow the form factor to be scaled on a point-by-point basis for increased accuracy.
- *The temperature factors (Beq) are fixed at default values.* This was done for simplicity's sake. Allowing the temperature factors to refine usually led to runaway fits that made little physical sense. Temperature factors may have a significant effect on the relative reflection intensities of an individual phase; a better understanding of how temperature factors behave in ultrasmall nanoparticle crystallite domains is needed.
- *Fluorescence*. Fluorescence adds another level of complexity to the analysis. The impact of fluorescence on a diffractogram is observed as an angle-independent vertical offset, as long as a constant sample volume is illuminated by the x-ray beam. The magnitude of the offset depends on the quantity and identity of the fluorescent element, and on the wavelength used. The assumption of constant illuminated volume means that fluorescence is also impacted by beam spill and finite sample thickness, therefore corrections for fluorescence must account for these intensity effects. Whether or not an element fluoresces in the XRD depends directly on the wavelength of x-rays used. A rule of thumb for determining the possibility of fluorescence using the periodic table is as follows: for a given x-ray source element, the elements to the left of the source element in the periodic table will fluoresce (excluding the element directly next to the source element). For example, if a copper x-ray source is used, then cobalt will have the greatest amount of fluorescence, followed by iron, manganese, chromium, vanadium, titanium, and so on. In practice, if a monochromator is not used then the x-ray source element and the element immediately to the left of the source element (in this example, copper and nickel) will also exhibit fluorescence due to the Bremsstrahlung radiation given off by the source. The most accurate way to address fluorescence is to avoid it completely by using an x-ray source that will not cause samples to fluoresce. However, this may not be possible for all research setups. Future work is needed to address the complexities of this issue, for more details see Lipp [51].

Conclusion

Bragg diffraction via benchtop XRD can be used to characterize sub-nm crystallites – much smaller than what is commonly reported in the literature. Characterization is possible even when multiple phases are present – i.e. the particles do not need to be fully reduced. This increased ability of XRD is afforded by the careful accounting of intensity effects and is further enhanced by the enhanced signal-to-noise provided by solid state detectors. Using the methods presented in this work, it is shown that < 2nm Pt / SiO_2 nanoparticles spontaneously oxidize to form a metallic core with PtO_2 shell; XRD analysis suggests that the metallic Pt core undergoes lattice dilation. These results demonstrate the ability of Bragg diffraction via Rietveld refinement to provide useful information for the characterization of sub-nm crystallites.

Acknowledgements

Leandro (Andy) DeCastro for filming the sample prep method

Magnus J. Lipp, for helpful discussions, advice, mathematical insight, and proofreading

Funding from the National Science Foundation IGERT program (Award Number 1250052)

South Carolina Smart State Center of Catalysis for Renewable Fuels (CReF)

Supporting Information

Supporting Information Available:

- *Supplementary Information.docx*
  Discussions for statistical errors, choosing crystalline references, detailed experimental methods (including notes on peak broadening), beam spill derivations, and Topas macro modifications
- *Cu_K_alpha_x-ray_mass_absorption_calculator.xlsx*
  Tool for calculating x-ray mass attenuation and absorption coefficients of supported materials
- *XRD sample prep introduction.mp4*
  Video introducing the series of videos on XRD sample preparation
- *Grinding XRD samples.mp4*
  Video detailing how to grind samples in preparation for nano-scale XRD
- *XRD Sample Prep Part 1.mp4*
  Video detailing the setup and first four steps of preparing a pre-ground sample for nano-scale XRD
- *XRD Sample Prep Part 2.mp4*
  Video detailing the final four steps of preparing a pre-ground sample for nano-scale XRD
- *Pt_11-17-20 LI-DC-AVG pos 2 errors shift cps.txt*
  Tab-delimited text file containing the 6-run average intensity (counts / s) vs 2θ (°) information of the 4.8% Pt / silica case study sample with calculated statistical errors (Note: change file extension to .xye for importing into Topas)

- *Pure A300_Pt LI-DC-AVG pos 2.txt*
  Tab-delimited text file containing the 6-run average intensity (counts / s) vs 2θ (°) information of the pure silica case study sample
- *Pure A300_Pt LI-DC-AVG pos 2 XMA-FT-VT.txt*
  Tab-delimited text file containing the 6-run average intensity (counts / s) vs 2θ (°) information of the pure silica case study sample after correcting for x-ray mass absorption, finite thickness, and total volume (Note: change file extension to .xy for importing into Topas)
- *Pt_11-17-20_chebychev_BKG_sub_A300_total_V_1_06_cps.txt*
  Tab-delimited text file containing the 6-run average intensity (counts / s) vs 2θ (°) information of the background subtracted 4.8% Pt / silica case study sample with calculated statistical errors
  (Note: change file extension to .xye for importing into Topas)
- *CIP Mendenhall Pt 11-17-20 cps to Pure A300_Pt 2-7-21 BKG sub total V ratio 1_06 xye fit 2 sigma.txt*
  Topas input file for the Rietveld analysis of the best fit shown in Figure 15, using the background subtracted 4.8% Pt / silica case study sample with calculated statistical errors (Note: change file extension to .INP for importing into Topas)
- *Fit 2 report.txt*
  Text file containing the Topas generated report for the best fit shown in Figure 15, including parameter values and errors (for refined values)

This material is available free of charge *via* the internet at http://pubs.acs.org.

References

1. Wong, A.; Liu, Q.; Griffin, S.; Nicholls, A.; Regalbuto, J., Synthesis of ultrasmall, homogeneously alloyed, bimetallic nanoparticles on silica supports. *Science* **2017,** *358* (6369), 1427-1430.

2. Miller, J.; Kropf, A.; Zha, Y.; Regalbuto, J.; Delannoy, L.; Louis, C.; Bus, E.; van Bokhoven, J. A., The effect of gold particle size on AuAu bond length and reactivity toward oxygen in supported catalysts. *Journal of Catalysis* **2006,** *240* (2), 222-234.

3. Gallagher, J. R.; Li, T.; Zhao, H.; Liu, J.; Lei, Y.; Zhang, X.; Ren, Y.; Elam, J. W.; Meyer, R. J.; Winans, R. E., In situ diffraction of highly dispersed supported platinum nanoparticles. *Catalysis Science & Technology* **2014,** *4* (9), 3053-3063.

4. O'Connell, K.; Regalbuto, J. R., High sensitivity silicon slit detectors for 1 nm powder XRD size detection limit. *Catalysis Letters* **2015,** *145* (3), 777-783.

5. Bazin, D.; Guczi, L.; Lynch, J., Anomalous wide angle X-ray scattering (AWAXS) and heterogeneous catalysts. *Applied Catalysis A: General* **2002,** *226* (1-2), 87-113.

6. Cromer, D. T.; Liberman, D., Relativistic calculation of anomalous scattering factors for X rays. *The Journal of Chemical Physics* **1970,** *53* (5), 1891-1898.

7. Cromer, D. T.; Liberman, D. A., Anomalous dispersion calculations near to and on the long-wavelength side of an absorption edge. *Acta Crystallographica Section A: Crystal Physics, Diffraction, Theoretical and General Crystallography* **1981,** *37* (2), 267-268.

8. Gallezot, P.; Avalos-Borja, M.; Poppa, H.; Heinemann, K., Structure and morphology characterization of nanometer-size metal aggregates by electron scattering patterns. *Langmuir* **1985,** *1* (3), 342-347.

9. Vogel, W.; Sachtler, W.; Zhang, Z., Formation of Metal Clusters in Zeolites Studied by Differential X-Ray Scattering. *Berichte der Bunsengesellschaft für physikalische Chemie* **1993,** *97* (3), 280-285.

10. Gnutzmann, V.; Vogel, W., Structural sensitivity of the standard platinum/silica catalyst EuroPt-1 to hydrogen and oxygen exposure by in situ X-ray diffraction. *Journal of Physical Chemistry* **1990,** *94* (12), 4991-4997.

11. Vogel, W.; Le Rhun, V.; Garnier, E.; Alonso-Vante, N., Ru clusters synthesized chemically from dissolved carbonyl: in situ study of a novel electrocatalyst in the gas phase and in electrochemical environment. *The Journal of Physical Chemistry B* **2001,** *105* (22), 5238-5243.

12. Vogel, W., Size contraction in Pt/C and PtRu/C commercial E-TEK electrocatalysts: An in situ X-ray diffraction study. *The Journal of Physical Chemistry C* **2008,** *112* (35), 13475-13482.

13. *TOPAS*, V.6.0; Bruker AXS: 2018.

14. Hubbel, J. H.; Seltzer, S. M., X-ray mass attenuation coefficients: NIST standard reference database 126. NIST: 2004.

15. Hermann, H.; Ermrich, M., Microabsorption correction of X-ray intensities diffracted by multiphase powder specimens. *Powder diffraction* **1989,** *4* (4), 189-195.

16. Zevin, L. S.; Kimmel, G.; Mureinik, I., Methodology of quantitative phase analysis. In *Quantitative X-Ray Diffractometry*, Springer: 1995; pp 100-225.

17. Brindley, G. W., XLV. The effect of grain or particle size on x-ray reflections from mixed powders and alloys, considered in relation to the quantitative determination of crystalline substances by x-ray methods. *The London, Edinburgh, and Dublin Philosophical Magazine and Journal of Science* **1945,** *36* (256), 347-369.

18. Dinnebier, R. E.; Leineweber, A.; Evans, J. S. O., *Rietveld Refinement: Practical Powder Diffraction Pattern Analysis Using Topas*. Walter de Gruyter GmbH: Berlin/Boston, 2019.

19. Pecharsky, V. K.; Zavalij, P. Y., *Fundamentals of Powder Diffraction and Structural Characterization of Materials*. 2nd ed.; Springer: 2009.

20. Pitschke, W.; Mattern, N.; Hermann, H., Incorporation of microabsorption corrections into Rietveid analysis. *Powder Diffraction* **1993,** *8* (4), 223-228.

21. Hermann, H.; Ermrich, M., Microabsorption of X-ray intensity in randomly packed powder specimens. *Acta Crystallographica Section A: Foundations of Crystallography* **1987,** *43* (3), 401-405.

22. Harrison, R. J.; Paskin, A., The effects of granularity on the diffracted intensity in powders. *Acta Crystallographica* **1964,** *17* (4), 325-331.

23. Suortti, P., Effects of porosity and surface roughness on the X-ray intensity reflected from a powder specimen. *Journal of Applied Crystallography* **1972,** *5* (5), 325-331.

24. Pitschke, W.; Hermann, H.; Mattern, N., The influence of surface roughness on diffracted X-ray intensities in Bragg–Brentano geometry and its effect on the structure determination by means of Rietveld analysis. *Powder Diffraction* **1993,** *8* (2), 74-83.

25. McCusker, L.; Von Dreele, R.; Cox, D.; Louër, D.; Scardi, P., Rietveld refinement guidelines. *Journal of Applied Crystallography* **1999,** *32* (1), 36-50.

26. Lipp, J.; Coelho, A., Topas V6 GUI does not read error column from .xye files? How can I input error information? In *Forum>Topas*, Topas Forum: 2022.

27. Schreier, M.; Regalbuto, J. R., A fundamental study of Pt tetraammine impregnation of silica: 1. The electrostatic nature of platinum adsorption. *Journal of Catalysis* **2004,** *225* (1), 190-202.

28. Miller, J. T.; Schreier, M.; Kropf, A. J.; Regalbuto, J. R., A fundamental study of platinum tetraammine impregnation of silica: 2. The effect of method of preparation, loading, and calcination temperature on (reduced) particle size. *Journal of Catalysis* **2004,** *225* (1), 203-212.

29. Xia, Y.; Harrison, P.; Ornelas, I.; Wang, H.; Li, Z., HAADF-STEM image analysis for size-selected platinum nanoclusters. *Journal of microscopy* **2020,** *279* (3), 229-233.

30. Wojdyr, M., Fityk: a general-purpose peak fitting program. *Journal of Applied Crystallography* **2010,** *43* (5-1), 1126-1128.

31. Owen, E.; Yates, E., XLI. Precision measurements of crystal parameters. *The London, Edinburgh, and Dublin Philosophical Magazine and Journal of Science* **1933,** *15* (98), 472-488.

32. Moore Jr, W. J.; Pauling, L., The crystal structures of the tetragonal monoxides of lead, tin, palladium, and platinum. *Journal of the American Chemical Society* **1941,** *63* (5), 1392-1394.

33. Kumar, J.; Saxena, R., Formation of NaCl-and Cu2O-type oxides of platinum and palladium on carbon and alumina support films. *Journal of the Less Common Metals* **1989,** *147* (1), 59-71.

34. Range, K.-J.; Rau, F.; Klement, U.; Heyns, A., β-PtO2: high pressure synthesis of single crystals and structure refinement. *Materials research bulletin* **1987,** *22* (11), 1541-1547.

35. Fernandez, M. H.; Chamberland, B., A new high pressure form of PtO2. *Journal of the Less Common Metals* **1984,** *99* (1), 99-105.

36. Hoekstra, H. R.; Siegel, S.; Gallagher, F. X., Reaction of platinum dioxide with some metal oxides. In *Platinum Group Metals and Compounds*, Rao, U. V., Ed. ACS Publications: 1971; pp 39-53.

37. Shirako, Y.; Wang, X.; Tsujimoto, Y.; Tanaka, K.; Guo, Y.; Matsushita, Y.; Nemoto, Y.; Katsuya, Y.; Shi, Y.; Mori, D., Synthesis, crystal structure, and electronic properties of high-pressure PdF2-type oxides MO2 (M= Ru, Rh, Os, Ir, Pt). *Inorganic chemistry* **2014,** *53* (21), 11616-11625.

38. Muller, O.; Roy, R., Formation and stability of the platinum and rhodium oxides at high oxygen pressures and the structures of Pt3O4, β-PtO2 and RhO2. *Journal of the Less Common Metals* **1968,** *16* (2), 129-146.

39. Galloni, E. E.; Roffo Jr, A. E., The crystalline structure of Pt3O4. *The Journal of Chemical Physics* **1941,** *9* (12), 875-877.

40. Grande, B.; Müller-Buschbaum, H., Ein Beitrag zu Verbindungen vom Typ MexPt3O4. *Journal of Inorganic and Nuclear Chemistry* **1977,** *39* (6), 1084-1085.

41. Bucher, J.; Buttet, J.; Van der Klink, J.; Graetzel, M., Electronic properties and local densities of states in clean and hydrogen covered Pt particles. *Surface Science* **1989,** *214* (3), 347-357.

42. Banerjee, R.; Liu, Q.; Tengco, J. M. M.; Regalbuto, J. R., Detection of Ambient Oxidation of Ultrasmall Supported Platinum Nanoparticles with Benchtop Powder X-Ray Diffraction. *Catalysis Letters* **2017,** *147* (7), 1754-1764.

43. Lamber, R.; Wetjen, S.; Jaeger, N. I., Size dependence of the lattice parameter of small palladium particles. *Physical Review B* **1995,** *51* (16), 10968.

44. Goyhenex, C.; Henry, C.; Urban, J., In-situ measurements of the lattice parameter of supported palladium clusters. *Philosophical Magazine A* **1994,** *69* (6), 1073-1084.

45. Jacobs, J.; Schryvers, D., A high-resolution electron microscopy study of photodeposited Pd particles on TiO2 and their oxidation in air. *Journal of Catalysis* **1987,** *103* (2), 436-449.

46. Du, K.; Ernst, F.; Pelsozy, M.; Barthel, J.; Tillmann, K., Expansion of interatomic distances in platinum catalyst nanoparticles. *Acta materialia* **2010,** *58* (3), 836-845.

47. Jentys, A., Estimation of mean size and shape of small metal particles by EXAFS. *Physical Chemistry Chemical Physics* **1999,** *1* (17), 4059-4063.

48. Wu, Z.; Wegener, E. C.; Tseng, H.-T.; Gallagher, J. R.; Harris, J. W.; Diaz, R. E.; Ren, Y.; Ribeiro, F. H.; Miller, J. T., Pd–In intermetallic alloy nanoparticles: highly selective ethane dehydrogenation catalysts. *Catalysis Science & Technology* **2016,** *6* (18), 6965-6976.

49. Ma, Z.; Wu, Z.; Miller, J. T., Effect of Cu content on the bimetallic Pt–Cu catalysts for propane dehydrogenation. *Catalysis, Structure & Reactivity* **2017,** *3* (1-2), 43-53.

50. Wu, Z.; Bukowski, B. C.; Li, Z.; Milligan, C.; Zhou, L.; Ma, T.; Wu, Y.; Ren, Y.; Ribeiro, F. H.; Delgass, W. N., Changes in catalytic and adsorptive properties of 2 nm Pt3Mn nanoparticles by subsurface atoms. *Journal of the American Chemical Society* **2018,** *140* (44), 14870-14877.

51. Lipp, J. W. Fine Points for Broad Bumps: the Extension of Rietveld Refinement for Benchtop Powder XRD Analysis of Ultra-small Supported Nanoparticles. University of South Carolina, 2021.

52. Bertolotti, F.; Moscheni, D.; Guagliardi, A.; Masciocchi, N., When Crystals Go Nano–The Role of Advanced X-ray Total Scattering Methods in Nanotechnology. *European Journal of Inorganic Chemistry* **2018,** *2018* (34), 3789-3803.

53. Pakharukova, V. P.; Yatsenko, D. A.; Gerasimov, E. Y.; Vlasova, E.; Bukhtiyarova, G. A.; Tsybulya, S. V., Total Scattering Debye Function Analysis: Effective Approach for Structural Studies of Supported MoS2-Based Hydrotreating Catalysts. *Industrial & Engineering Chemistry Research* **2020,** *59* (23), 10914-10922.

54. Kaszkur, Z. In *Test of applicability of some powder diffraction tools to nanocrystals*, Ninth European Powder Diffraction Conference, Oldenbourg Wissenschaftsverlag: 2015; pp 147-154.

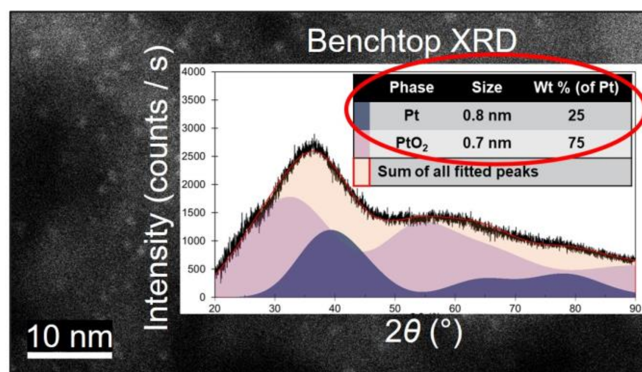

Figure 19. TOC Graphic